

DESIGN OF SPIRAL ANTENNA ARRAY  
AND COMMUNICATION SYSTEM FOR X-BAND CUBESAT IN LUNAR ORBIT

by

KATELYN ROSE ISBELL

YANG-KI HONG, COMMITTEE CHAIR

STEPHEN J. YAN

SEVGI GURBUZ

RICHARD D. BRANAM

A THESIS

Submitted in partial fulfillment of the requirements  
for the degree of Master of Science  
in the Department of Electrical and Computer Engineering  
in the Graduate School of  
The University of Alabama

TUSCALOOSA, ALABAMA

2020

Copyright Katelyn Rose Isbell 2020  
ALL RIGHTS RESERVED

## ABSTRACT

Recent advancements in the design of CubeSats, a type of nanosatellite, have allowed missions to include lunar, asteroid, and planetary destinations. Communication for deep space CubeSats poses new challenges for researchers in terms of transmitting and receiving range capabilities, reliability, and power and size limitations. An X-band downlink communication system is designed to address link budget and CubeSat system requirements for a lunar orbit. An Archimedean spiral antenna array backed by a novel sloped wall cavity and fed with a Klopfenstein impedance taper and power splitter is designed and characterized. An X-band transmitter is designed to fulfill the link budget and is analyzed for RF performance.

## DEDICATION

This thesis is dedicated to my parents for their endless support.

## LIST OF ABBREVIATIONS AND SYMBOLS

ADS	Advanced Design System
AR	Axial Ratio
AR <sub>00</sub>	Axial Ratio at Boresight
ARBW	Axial Ratio Beam Width
ASA	Archimedean Spiral Antenna
BER	Bit Error Rate
BPSK	Binary Phase Shift Keying
CBC	Conventional Backing Cavity
COTS	Commercial Off-the-Shelf
D	Distance in Link Budget
DAC	Digital-to-Analog Converter
DSN	Deep Space Network
DSP	Digital Signal Processing
$E_b$	Energy Per Bit
EM-1	Exploration Mission-1
ESA	European Space Administration
FCC	Federal Communications Commission
FPGA	Field Programmable Gate Array
FQPSK	Feher Patented Quadrature Phase-Shift Keying

FSPL	Free Space Path Loss
GMSK	Gaussian Minimum Shift Keying
$G_R$	Receiving Antenna Gain
$G_T$	Transmitting Antenna Gain
HFSS	High Frequency Structure Simulator
HGA	High Gain Antenna
HPBW	Half Power Beam Width
I	In-Phase
INSPIRE	Interplanetary Nano-Spacecraft Pathfinder in Relevant Environment
JPL	Jet Propulsion Laboratory
LEO	Low Earth Orbit
LGA	Low Gain Antenna
MarCO	Mars Cube One
MGA	Medium Gain Antenna
$N_0$	Noise Spectral Density
NASA	National Air and Space Administration
OQPSK	Offset Quadrature Phase Shift Keying
P-POD	Poly-Picosatellite Orbital Deployer
$P_R$	Receiving Power
PSK	Phase-Shift Keying
$P_T$	Transmitting Power
Q	Quadrature
QPSK	Quadrature Phase Shifting Keying

R	Data Rate
RF	Radio Frequency
RG	Realized Gain
RG <sub>00</sub>	Realized Gain at Boresight
RX	Receive
SCRAM	Space Communication Rates At Multi-Gbps
SFDR	Spurious-Free Dynamic range
SNR	Signal to Noise Ratio
SQPSK	Staggered Quadrature Phase-Shift Keying
SWBC	Sloped-Wall Backing Cavity
T <sub>s</sub>	System Noise Temperature
TX	Transmit
UHF	Ultra-High Frequency
VHF	Very High Frequency
VNA	Vector Network Analyzer
Z <sub>0</sub>	Initial Impedance
Z <sub>in</sub>	Input Impedance
Z <sub>L</sub>	Load Impedance
ε <sub>eff</sub>	Effective Relative Permittivity
ε <sub>r</sub>	Relative Permittivity
Γ	Reflection Coefficient

## ACKNOWLEDGEMENTS

I would like to thank my advisor and committee chair, Dr. Yang-Ki Hong for his guidance and support for my graduate and undergraduate research careers. I would also like to thank my committee members Dr. Stephen J. Yan, Dr. Sevgi Gurbuz, and Dr. Richard D. Branam for their help in my completion of this thesis. I am also grateful to my fellow researchers in the Magnetic Materials and Devices lab for their assistance: Dr. Woncheol Lee, Nikolaus Luhrs, Hoyun Won, Minyeong Choi, Briana Bryant, Jonathan Platt, and Leo Vanderburgh.

## CONTENTS

ABSTRACT.....	ii
DEDICATION.....	iii
LIST OF ABBREVIATIONS AND SYMBOLS.....	iv
ACKNOWLEDGEMENTS.....	vii
LIST OF TABLES.....	xi
LIST OF FIGURES.....	xii
CHAPTER 1: INTRODUCTION.....	1
1.1 Motivation.....	1
1.2 Contributions.....	1
1.3 Organization.....	2
1.4 Publications.....	2
CHAPTER 2: LITERATURE REVIEW.....	5
2.1 History of CubeSats.....	5
2.2 The CubeSat Standard.....	7
2.3 CubeSats for Deep Space.....	8
CHAPTER 3: SYSTEM OVERVIEW.....	12
3.1 Mission.....	12

3.2 Proposed System .....	12
3.3 Modulation Selection .....	14
3.4 Frequency Band Selection.....	16
3.5 Link Budget.....	16
3.6 Bandwidth .....	19
CHAPTER 4: ANTENNA DESIGN .....	21
4.1 Antenna Characteristics.....	21
4.2 Archimedean Spiral.....	22
4.2.1 Theory of Operation.....	22
4.2.2 Design .....	24
4.3 Microstrip Balun .....	26
4.3.1 Theory of Operation.....	26
4.3.2 Design .....	27
4.3.3 Fabrication and Measurement.....	33
4.4 Backing Cavity .....	36
4.4.1 Theory of Operation.....	36
4.4.2 Design .....	37
4.5 Spiral Array .....	41
4.5.1 Design .....	41
4.5.2 Proposed 6x6 Spiral Array.....	43

4.6 Power Splitter .....	43
4.6.1 Theory of Operation.....	43
4.6.2 Design .....	44
4.7 Antenna Characterization.....	49
4.7.1 Fabrication Process .....	49
4.7.2 Measurement Process.....	49
4.7.3 Spiral Antennas.....	51
4.7.4 Arrays.....	55
CHAPTER 5: TRANSMITTER DESIGN.....	59
5.1 Modulation .....	60
5.2 Digital to Analog Converter.....	62
5.3 Upconversion .....	62
5.4 Amplification .....	63
CHAPTER 6: CONCLUSION .....	64
REFERENCES .....	66

## LIST OF TABLES

Table 1. Current Deep Space Network Goldstone antenna downlink capabilities .....	16
Table 2. System noise temperature of Deep Space Network antennas .....	17
Table 3. Required received powers of Deep Space Network antenna for OQPSK .....	18
Table 4. Friis equation for downlink from CubeSat to earth .....	18
Table 5. Impedances for multi-section binomial Wilkinson power dividers.....	45
Table 6. Dimensions of multi-section binomial Wilkinson power dividers on FR4 substrate .....	46

## LIST OF FIGURES

Figure 1. Diagram of 1U, 3U, and 6U CubeSats .....	5
Figure 2. CubeSats launched each year since 1998 according to the Nanosats Database [9] .....	7
Figure 3. NASA’s deep space CubeSat, MarCO, with reflectarray and UHF antenna [2].....	10
Figure 4. Proposed mission for 6U CubeSat communication relay in lunar orbit.....	13
Figure 5. Proposed 6U CubeSat for communication relay in lunar orbit .....	13
Figure 6. QPSK modulation block diagram.....	15
Figure 7. OQPSK modulation block diagram.....	15
Figure 8. Archimedean spiral generated in MATLAB with $a = 1$ and $b = 2$ for $\theta = 0$ to $2\pi$ .....	23
Figure 9. Surface current distribution of two-arm Archimedean spiral antenna .....	23
Figure 10. The two-arm Archimedean spiral antenna .....	24
Figure 11. The (a) radiation pattern and (b) axial ratio pattern of the two-arm Archimedean spiral antenna at 8.45 GHz.....	25
Figure 12. The (a) reflection coefficient and radiation efficiency and (b) realized gain and axial ratio as a function of frequency of the two-arm Archimedean spiral antenna .....	26
Figure 13. Impedance tapers for transition from 50 to 170 $\Omega$ .....	28
Figure 14. Microstrip impedance transformers: (a) Klopfenstein, (b) linear, and (c) exponential tapers .....	30
Figure 15. Simulated reflection coefficient of microstrip impedance tapers .....	31
Figure 16. Transversal cut of asymmetrical double-sided strip lines .....	31
Figure 17. Designed back-to-back Klopfenstein balun on Rogers RT/duroid 5880.....	33
Figure 18. Reflection coefficient of Klopfenstein balun with 20 mm parallel stripline extension .....	33
Figure 19. Fabricated back-to-back microstrip impedance transformer on Rogers RT/duroid 5880.....	34

Figure 20. Measurement setup of S-parameters using Agilent Vector Network Analyzer N5230A.....	34
Figure 21. Measured and simulated S-parameters of back-to-back microstrip impedance transformer ( $L = 20$ mm, Klopfenstein taper, Rogers RT/duroid 5880).....	35
Figure 22. Fabricated back-to-back Klopfenstein balun.....	35
Figure 23. Measured and simulated S-parameters of back-to-back Klopfenstein balun .....	36
Figure 24. Backing cavity for Archimedean spiral antenna .....	37
Figure 25. Effect of cavity height on realized gain at boresight of Archimedean spiral antenna ..	38
Figure 26. Effect of cavity height on axial ratio at boresight of Archimedean spiral antenna.....	38
Figure 27. Sloped wall backing cavity for Archimedean spiral antenna .....	39
Figure 28. Effect of lower radius of sloped wall backing cavity on realized gain at boresight of the Archimedean spiral antenna .....	40
Figure 29. Realized gain and axial ratio at boresight of Archimedean spirals antennas with (i) no backing cavity, (ii) conventional backing cavity with 6 mm height, and (iii) sloped wall backing cavity .....	41
Figure 30. The 4 x 4 Archimedean spiral antenna array on 1U CubeSat face (100 cm x 100 cm) .....	42
Figure 31. Realized gain and axial ratio at boresight of 4 x 4 Archimedean spiral antenna array with (i) no backing cavity, (ii) conventional backing cavity and (iii) sloped wall backing cavity .....	42
Figure 32. Proposed deployable sloped wall cavity-backed Archimedean antenna array.....	43
Figure 33. Circuit implementation of the Wilkinson power splitter.....	44
Figure 34. Binomial power splitter on Rogers RT/duroid 5880: (a) diagram and (b) simulated S-parameters .....	44
Figure 35. Multi-section Wilkinson power splitter.....	45
Figure 36. Multi-section binomial Wilkinson power dividers on FR4 substrate with sections of (a) 1, (b) 2 and (c) 3.....	46
Figure 37. Reflection coefficient of binomial Wilkinson power dividers with number of sections of 1, 2, and 3.....	47
Figure 38. Binomial Wilkinson power divider with three sections: (a) simulated and measured S-parameters and (b) fabricated prototype .....	48

Figure 39. A binomial (3 section) Wilkinson power splitter with four outputs: (a) simulated S-parameters and (b) microstrip implementation .....	48
Figure 40. Fabricated copper cavities using (a) electroplating and (b) copper tape .....	49
Figure 41. Set-up of Anechoic Chamber (Quietbox AVS 700) for radiation characterization ....	50
Figure 42. Archimedean spiral antenna: (a) fabricated prototype and (b) measured and simulated reflection coefficient.....	52
Figure 43. Measured and simulated (a) realized gain and (b) axial ratio at boresight of the Archimedean spiral antenna.....	53
Figure 44. Archimedean spiral antenna with sloped wall backing cavity: (a) fabricated prototype and (b) measured and simulated reflection coefficient.....	54
Figure 45. Measured and simulated (a) realized gain and (b) axial ratio at boresight of the Archimedean spiral antenna with sloped wall backing cavity .....	54
Figure 46. Measured and simulated realized gain radiation pattern as a function of $\theta$ at $\phi = 0^\circ$ of the Archimedean spiral antenna with sloped wall backing cavity.....	55
Figure 47. Archimedean spiral antenna array (a) prototype and (b) measured and simulated reflection coefficient .....	56
Figure 48. Measured and simulated (a) realized gain and (b) axial ratio at boresight of the Archimedean spiral antenna array .....	56
Figure 49. Archimedean spiral antenna array with sloped wall backing cavity: (a) prototype and (b) measured and simulated reflection coefficient .....	57
Figure 50. Measured and simulated (a) realized gain and (b) axial ratio at boresight of the Archimedean spiral antenna array with sloped wall backing cavity.....	58
Figure 51. Measured and simulated realized gain radiation pattern of the Archimedean spiral antenna array with sloped wall backing cavity .....	58
Figure 52. X-band transmitter schematic employing direct frequency conversion .....	60
Figure 53. ADS implementation of OQPSK modulation .....	61
Figure 54. OQPSK simulation results for (a) spectrum of generated signal, (b) trajectory diagram, and (c) real part of modulated RF carrier versus time. ....	61
Figure 55. Simulated spectrum of (a) input and (b) output voltages of the ideal direct frequency conversion X-Band transmitter in ADS .....	63

## CHAPTER 1: INTRODUCTION

### 1.1 Motivation

The development of small satellites is critical to the advancement of satellite technology. While the cost of launching a conventional satellite ranges from \$10 million to \$400 million [1], small satellites can be launched at a fraction of the cost. Lower cost risk and faster development time allows developers to design with less margin. Thus, the low risk and size restrictions encourage the miniaturization of electronics, optimization of system space and resources, and novel inventions. CubeSats, small satellites based on a standard originally developed for student-led projects, are leading the way in these developments. Although CubeSats began as basic amateur-level satellites in 1999, they are being increasingly utilized for more complex missions. As of 2018, CubeSats have even been deployed to deep space [2]. These deep space CubeSats push the boundaries of miniature satellite development, especially in the field of communications. They function as communication relays, imagers, and platforms for experimental technology at a fraction of the cost, size, and development time of a conventional deep space satellite. The demand for high quality and reliable communication link for the deep space CubeSats is especially important and is investigated in this thesis.

### 1.2 Contributions

The objective of this thesis is to design a low-profile X-band downlink communication system for a CubeSat in lunar orbit. The contributions from this thesis are as follows:

- A communication link budget is evaluated based on CubeSat mission and Deep Space Network operation.

- The design process of a two-arm Archimedean Spiral for X-band operation and Klopfenstein taper is performed using ANSYS High Frequency Structure Simulator (HFSS).
- A novel sloped-wall backing cavity for the Archimedean spiral antenna is designed using HFSS.
- The design of a 4 x 4 antenna element array with backing cavity, balun, and power splitter is performed and verified.
- The fabrication and characterization of the designed antennas and antenna arrays is performed.
- An X-band transmitter is designed and verified using Keysight Advanced Design System (ADS).

### **1.3 Organization**

In Chapter 2, a brief literature survey is performed on the status of CubeSats deployed or scheduled to be deployed in deep space. In Chapter 3, the proposed CubeSat system is detailed, including the CubeSat mission, frequency selection, modulation selection, and link budget. In Chapter 4, the antenna array is designed, including the Archimedean spiral antenna, backing cavity, microstrip baluns, and power splitter. The fabrication of the antenna array is explained, and the measured results of the fabricated array are analyzed. In Chapter 5, the design of an X-band transmitter using commercial off-the-shelf (COTS) components are described. Lastly, concluding remarks are made, and notes are given on future work.

### **1.4 Publications**

Over the course of the author's undergraduate and graduate careers, the following publications, patents, and presented papers were produced.

### *Peer Reviewed Journals*

[1] Woncheol Lee, Nikolaus Luhrs, Katelyn Isbell, Cristion Oliphant-Jerry, Peyton Morris, and Yang-Ki Hong, "Cavity-Backed Archimedean Spiral Antenna with Conical Perturbations for 3U CubeSat Applications [Education Corner]," *IEEE Antennas and Propagation Magazine*, vol. 60, no. 6, pp. 102-109, Dec. 2018.

[2] Hoyun Won, Katelyn Isbell, Leo Vanderburgh, Jonathan Platt, Woncheol Lee, and Yang-Ki Hong, "Direction Finding System and Channel Sounder using a Pseudo-Doppler Antenna Array [Education Corner]," *IEEE Antennas and Propagation Magazine*, vol. 61, no. 4, pp. 84-89, Aug. 2019.

### *Provision Patent Applications*

[1] Yang-Ki Hong, Woncheol Lee, Katelyn Isbell, and Nikolaus Luhrs, "Cavity-backed Spiral Antenna with Perturbation Elements," filed on January 4, 2018, U.S. Patent Application No. 62/613,640.

[2] Yang-Ki Hong, Hoyun Won, Katelyn Isbell, Leo Vanderburgh, Jonathan Platt, and Woncheol Lee, "Method and System for Direction Finding and Channel Sounding System using Pseudo-Doppler Antenna Array," filed on Jul. 10, 2019. U.S. Application No. 62/872,509.

### *Presented Papers*

[1] Woncheol Lee, Yang-Ki Hong, Hoyun Won, Minyeong Choi, Katelyn Isbell, and Jaejin Lee, "High-gain Miniature Axial-mode Helical Antenna with Ferrite Loading," Paper No. CI-03, presented at the 62nd Magnetism and Magnetic Materials Conference, Pittsburgh, Pennsylvania, November 6 – 10, 2017.

[2] Woncheol Lee, Nikolaus Luhrs, Katelyn Isbell, Cristion Oliphant-Jerry, and Peyton Morris, "Cavity-Backed Archimedean Spiral Antenna with Conical Perturbations for 3U CubeSat Applications," Student Design Contest (1st place), presented at 2017 IEEE AP-S Symposium on Antennas and Propagation and USNC-URSI Radio Science Meeting, San Diego, California, July 9 – 14, 2017.

[3] Hoyun Won, Katelyn Isbell, Leo Vanderburgh, and Jonathan Platt, "Channel Sounder and Radiolocation System Using a Pseudo Doppler Antenna Array," Student Design Contest (2nd place), presented at 2018 IEEE AP-S Symposium on Antennas and Propagation and USNC-URSI Radio Science Meeting, Boston, Massachusetts, July 8 – 13, 2018.

[4] Katelyn Isbell, Yang-Ki Hong, Woncheol Lee, Hoyun Won, and Minyeong Choi, "X-band Archimedean Spiral Antenna Array with Sloped-Wall Backing Cavity," presented at 2019 IEEEAP-S Symposium on Antennas and Propagation and USNC-URSI Radio Science Meeting, Atlanta, Georgia, July 7 – 12, 2019.

*Awards/Grants*

[1] IEEE Antennas & Prop. Society Eugene F. Knott Memorial Pre-Doctoral Research Grant, awarded to proposal for “Archimedean Spiral Antenna with Backing Cavity for Deep Space CubeSats,” May 2018

## CHAPTER 2: LITERATURE REVIEW

### 2.1 History of CubeSats

In 1999, the California Polytechnic State University and Stanford University's Space Systems Development Lab developed a standard for universities to develop and deploy small satellites for Low Earth Orbit (LEO) [3]. The CubeSat standard was designed to allow fast and affordable development of a small satellite for educational applications. The main aspect of the standard is the basic unit volume of 1U, which describes a 10 cm x 10 cm x 10 cm cube. As shown in Figure 1, CubeSats of size 1U, 3U, 6U, and larger can be developed. Due to the size constraint, the small satellites can be deployed as secondary payloads on standardized ejectors or launched from the International Space Station, which reduces the cost of launch from the standard satellite cost of \$10 to 400 million [1] to as low as \$40,000 in LEO [4]. The standard also involves mass and power constraints, in addition to testing for space-readiness [5]. To achieve the fast development time, CubeSats are recommended to employ COTS components.

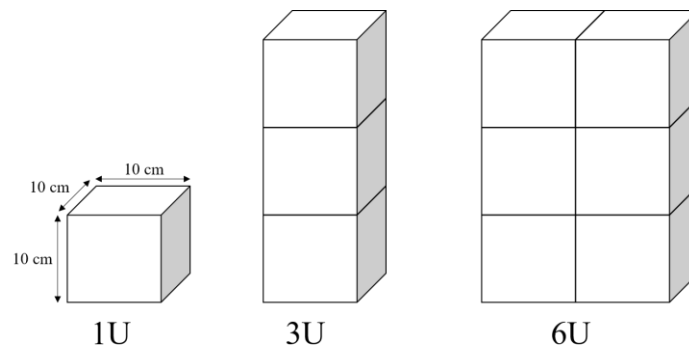


Figure 1. Diagram of 1U, 3U, and 6U CubeSats

In 2003, the first CubeSats, CanX-1, DTU sat-1, and AAU1 were successfully launched on a Russian Eurockot by the Space Flight Laboratory at the University of Toronto Institute for Aerospace Studies to demonstrate the operation of new on-board technology [6]. Following the initial launches, 100 CubeSats were launched from 2003 to 2012. A review of the first 100 CubeSats found most missions to be educational (37%), closely followed by technology (34%), science (23%), and lastly communication (6%) [7]. Of the first 100 CubeSats that reached their orbit, 40% failed to achieve their missions, with the failures mostly being attributed to lack of contact (45%), communication (17%) and power (17%).

Although CubeSats were initially perceived to be suitable only for amateur and educational applications, they quickly began to be used as versatile solutions for space applications. In addition to universities designing CubeSats with more complex systems, private companies and government agencies now utilize the CubeSats. A study of CubeSats from 2002 to 2018 reveals that the number of deployed CubeSats has approached 1000, including a significant increase in satellites devoted to remote sensing and science applications [8]. Over this period, more CubeSat users have shifted to be commercial enterprises, with the distribution being 57% commercial, 29% university, 7% military, and 7% civil as of May 2018. CubeSats are appealing to commercial and military users because they provide a much lower risk in comparison to standard satellites. As of January 2020, 1200 CubeSats have been launched as shown in Figure 2 [9].

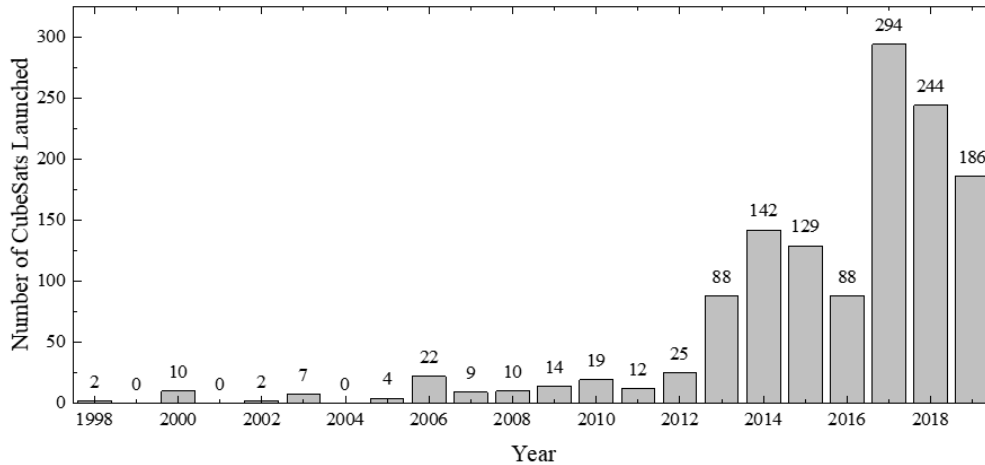


Figure 2. CubeSats launched each year since 1998 according to the Nanosats Database [9]

## 2.2 The CubeSat Standard

The CubeSat standards provides a guideline for satellite developers to ensure compatibility with standardized ejectors, with the original specification referring to the Poly-Picosatellite Orbital Deployer (P-POD) [5]. The CubeSat is required to remain intact during launch, ejection, and operation to ensure no space debris is created. Mechanical requirements include a maximum mass of 1.33 kg for 1U CubeSats (4.00 kg for 3U CubeSats) and constraints on the center of gravity. The electrical requirements include several fail-safe options, battery circuit protection, and RF power inhibitors. Testing requirements include random vibration, thermal vacuum bakeout, and shock testing. All materials used for the CubeSat system must satisfy NASA’s low out-gassing criterion.

Additionally, CubeSats are required to be properly licensed under the Federal Communications Commission (FCC). An experimental license is most commonly obtained for university-based CubeSats [10], which requires the communication system to operate on a non-interference basis with fully licensed systems, cease emissions if necessary, and limit emissions

in certain bands. The NASA CubeSat Launch Initiative recommends licensing procedures begin as soon as the CubeSat mission is determined [10].

### **2.3 CubeSats for Deep Space**

In May 2018, NASA deployed the first deep space CubeSats: Mars Cube One (MarCO), which were a pair of CubeSats launched with NASA's InSight Mars lander. From May 2018 to January 2019, MarCO functioned as a communication relay for the InSight during the entry, descent, and landing on Mars. The communications relay operated by receiving data in the UHF band from InSight and transmitting the data in the X-Band to the Deep Space Network (DSN) ground stations on earth. As of January 2020, MarCO are the only deep space CubeSats to be successfully deployed; although, several more are in development. For instance, the proposed Hera mission by the European Space Agency (ESA) will include two deep space CubeSats, which will travel with the Asteroid Prospection Explorer. The CubeSats will orbit an asteroid and transport a low-frequency radar and gravimeter to investigate the internal structure and gravity field of the asteroid [11]. Additionally, NASA's Artemis 1, a lunar orbital test flight, is scheduled to launch in 2021 and is expected to deploy 13 deep space CubeSats with similar capabilities to the MarCO [12].

Due to high gain requirements, deep space communications typically rely on higher bands such as X, K, and Ka where bandwidth is less limited and antenna size is reduced. The frequency band must be compatible with the DSN. The DSN consists of three base stations placed geometrically around the Earth. Conventionally, deep space communication systems employ high gain steerable horn antennas. For instance, the Voyager I, which is more than 13 billion miles from earth as of 2020, utilizes a 3.7 m high gain reflector antenna that operates in the X-band and S-band with data rates of 7.2 kb/s and 40 b/s, respectively [13]. In the case of

CubeSats, the complexity and weight added by a high gain horn antenna, steering and/or deployment system is undesirable.

For student and amateur CubeSat designers, operation at higher frequency bands poses a large challenge. CubeSat-compatible COTS transceivers are not available in X-band frequencies and higher. Therefore, modifications to existing systems or custom designs are required. Also, deep space CubeSats must undergo radiation hardening to protect against radiation events which cause damage to unprotected electronics. Requirements for deep space operation also include withstanding extreme temperature, achieving long life-times, and operating with proper propulsion [14].

Due to these challenges, research in deep space CubeSat communications has been mainly spearheaded by NASA Jet Propulsion Laboratory, especially in development of MarCO, which is displayed in Figure 3. The MarCO project involved the design of a deployable X-band reflectarray, deployable UHF circularly polarized loop, and custom transceiver. The UHF circularly polarized loop achieves an antenna gain of 5 dBi ( $> 0$  dBic at  $30^\circ$  off boresight) for communication between InSight and the MarCO. The deployable reflectarray is a transmit-only antenna with a gain of 29.2 dBic with 42% efficiency. It achieves downlink communication between the MarCO and the DSN at a distance of approximately 156 million km and data rate of 8 kb/s, even with the Iris radio amplifier limited to 5 W [12].

The custom transceiver, the Iris V2.1 CubeSat deep space Transponder, requires 0.5 U volume, has 1.2 kg mass, consumes a maximum of 35 W DC power, and operates at the DSN X-band frequencies of 7.2 GHz uplink and 8.4 GHz downlink [15]. Additional projects from JPL include the Interplanetary Nano-Spacecraft Pathfinder in Relevant Environment (INSPIRE) project and Lunar Flashlight. INSPIRE is a technology demonstration mission that aims to place

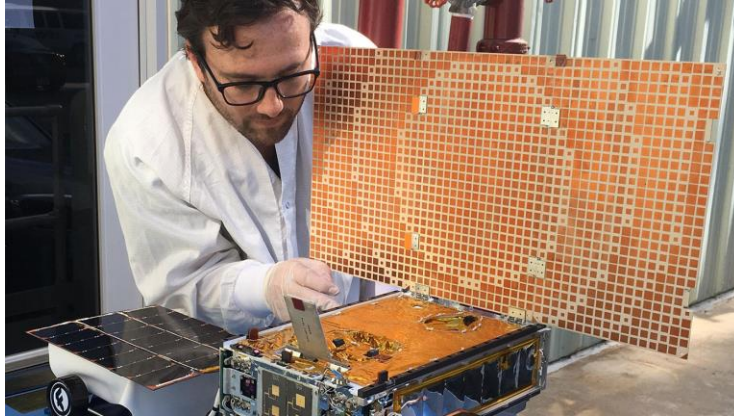


Figure 3. NASA's deep space CubeSat, MarCO, with reflectarray and UHF antenna [2]

a CubeSat in escape-earth orbit and will utilize the Iris X-band radio. The Lunar Flashlight will travel to the moon as a secondary payload on the Space Launch System's Artemis 1 flight in order to demonstrate green propulsion and to map the lunar south pole.

In addition to the reflectarrays deployed by the MarCO, many high gain antennas (HGA) are being developed for deep space CubeSats. For CubeSats with deployment capability or availability of large surface areas, HGA can be implemented. HGA include mesh reflectors, inflatables, membranes, slot arrays, and metasurface antennas [12]. LEO CubeSats typically implement low gain antennas (LGA) such as patches and wires. LGA are also useful for deep space communication in terms of short-distance intersatellite or CubeSat-lander communications. The medium gain antennas (MGA) are smaller in size but still achieve gains sufficient for CubeSat to ground communications. Unless the high gain of the HGA is required and the space is available, an MGA is highly recommended to reduce complexity of the system [12].

Medium gain antennas (MGAs) or patch antenna arrays are implemented when high gain is required but space is constrained to the CubeSat. The Near-Earth Asteroid Scout, Biosentinel, and CuSP missions to be deployed on NASA's Artemis 1 will all employ an MGA with a gain of 23.4 dBic for transmitting data to the DSN at a rate of 1-4 kb/s. The MGA consists of an 8 x 8

circularly polarized patch array mounted on a carbon-fiber deployable wing. In many cases, the MGA may be small enough to be mounted directly to the face of the CubeSat and the deployment system can be avoided. For instance, the Europa Lander mission employs an all-metal 8 x 8 patch array on the face of the CubeSat with a gain of 25.3 dBic for uplink and downlink with an efficiency of 80%. Additionally, metal-only metasurface antennas have been proposed to utilize the metal of the CubeSat [12].

## CHAPTER 3: SYSTEM OVERVIEW

### 3.1 Mission

In this section, the mission, proposed system, modulation selection, frequency band selection, link budget, and bandwidth will be discussed for the University of Alabama's deep space CubeSat communication system. The designed CubeSats will address the opportunity to map the moon and locate potentially viable locations for human habitation. For example, in 2009, the Selenological and Engineering Explorer for SELENE Terrain Camera [16] located a large deep pit (estimated at 65 m wide and 80 m deep) near the Marius Hills on the moon. The presence of this pit indicates possible lava tubes under the surface. The lava tubes have an estimated roof thickness of 10 meters, which would provide shielding from meteorites and radiation. Investigation of the lava tubes will (i) provide new information about the formation of the moon and (ii) be a potential location for safe human exploration and habitation. To further map the area, a lunar lander has been proposed to explore the lava tubes. To enable communications between the lander and earth, a 6U CubeSat will be utilized for communication relays, as shown in Figure 4. Additionally, the CubeSat will utilize imaging technology to aid in the 3D mapping with technology such as stereoscopic cameras, such as those used by the SELENE. Toward these aims, the CubeSat must be capable of uplink and downlink with the DSN and lunar lander.

### 3.2 Proposed System

The proposed CubeSat is 6U with maximum mass of 8 kg. The communication system enables VHF communication between the CubeSat and the lunar lander, as well as X-band

communication between the CubeSat and the DSN. Additionally, a stereoscopic camera will be used for data collection of the composition of the lunar surface [17]. For a comparable rate to the MarCO, the CubeSat communicates with the lunar lander and ground station at a rate of 8 kbps using VHF [2]. A conceptual depiction of the proposed CubeSat is given in Figure 5.

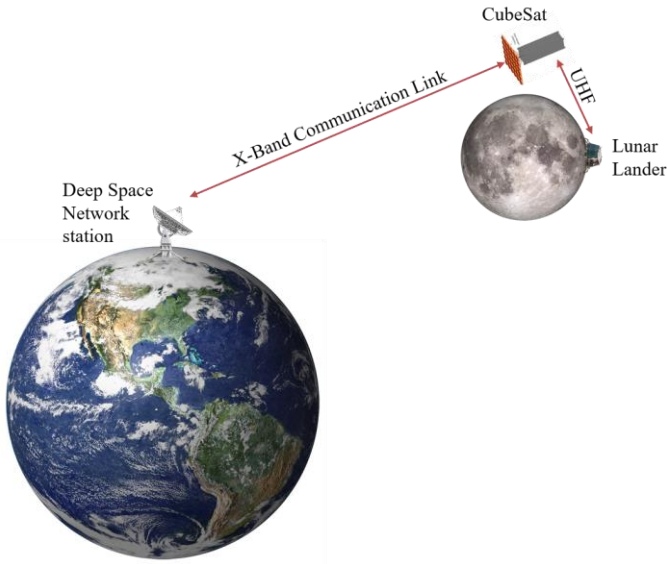


Figure 4. Proposed mission for 6U CubeSat communication relay in lunar orbit

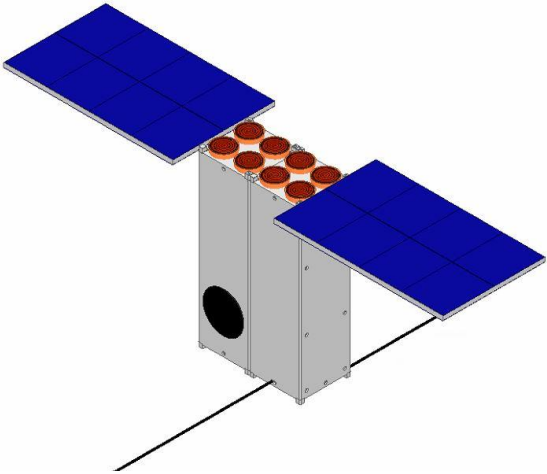


Figure 5. Proposed 6U CubeSat for communication relay in lunar orbit

### 3.3 Modulation Selection

To fulfill deep space requirements, it is recommended by the Consultative Committee for Space Data Systems that the modulation schemes of Gaussian Minimum Shift Keying (GMSK), Feher patented Quadrature Phase-Shift Keying (FQPSK), and Staggered Quadrature Phase-Shift Keying (SQPSK) be utilized [18]. The schemes are recommended due to their constant amplitude envelope, which allow for nonlinear amplifiers to be used to aid in power requirements. GMSK is a form of minimum shift keying with a Gaussian lowpass filter used to shape the waveform. It can be implemented with simple hardware as it relies on basic frequency modulation and has a constant amplitude envelope. Alternatively, Quadrature Phase-Shift Keying (QPSK) is a form of phase modulation that uses less bandwidth (spectral efficiency of 2 bps/Hz) compared to GMSK (spectral efficiency of 1.35 bps/Hz). QPSK is implemented by modulating two-bit data into the signal's phase,  $\phi(t)$ , where the phase can have values of  $45^\circ$ ,  $135^\circ$ ,  $225^\circ$ , or  $315^\circ$ , corresponding to data values of 00, 01, 10, or 11, respectively. The modulated signal,  $s(t)$ , has the form of [19]

$$s(t) = A_c \cos(2\pi f_c t + \phi(t)), \quad (3.1)$$

where  $f_c$  is the center frequency and  $A_c$  is the signal amplitude. The equation can be simplified to

$$s(t) = A_c \cos(2\pi f_c t) \cos(\phi(t)) - A_c \sin(2\pi f_c t) \sin(\phi(t)), \quad (3.2)$$

where the cosine term is the in-phase (I) signal, and the sine term is the quadrature (Q) signal.

Therefore, QPSK can be implemented with the block diagram in Figure 6. FQPSK and SQPSK are forms of Offset Quadrature Phase-Shift Keying (OQPSK), where the Q signal is delayed by one half the symbol period. The delay ensures that the maximum phase change at one point is  $90^\circ$ , while a total phase change of  $180^\circ$  is achieved during one symbol. SOQPSK and FQPSK are versions of OQPSK that use digital signal processing to shape the I and Q signals to have

smooth transitions. Additionally, the DSN supports the Phase-Shift Keying (PSK), Binary Phase-Shift keying (BPSK), QPSK, OQPSK modulation schemes. Due to DSN compatibility and the spectral efficiency, OQPSK is chosen as the modulation scheme. OQPSK can be implemented by using a simple hardware configuration, as shown in Figure 7.

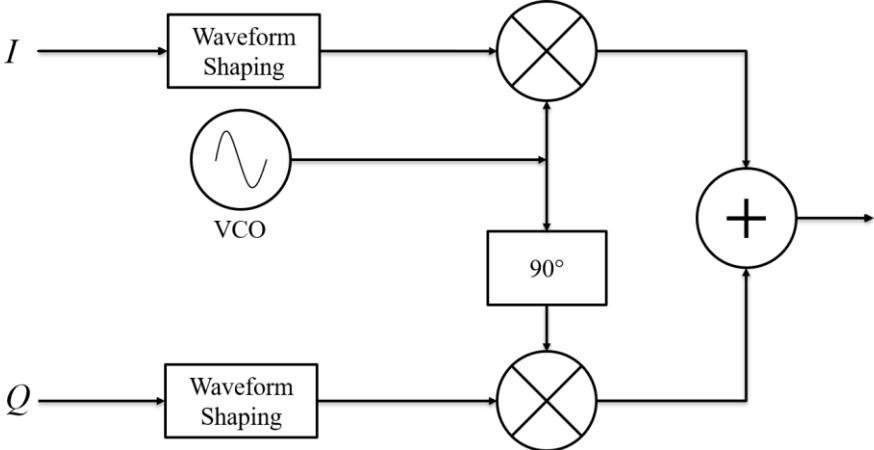


Figure 6. QPSK modulation block diagram

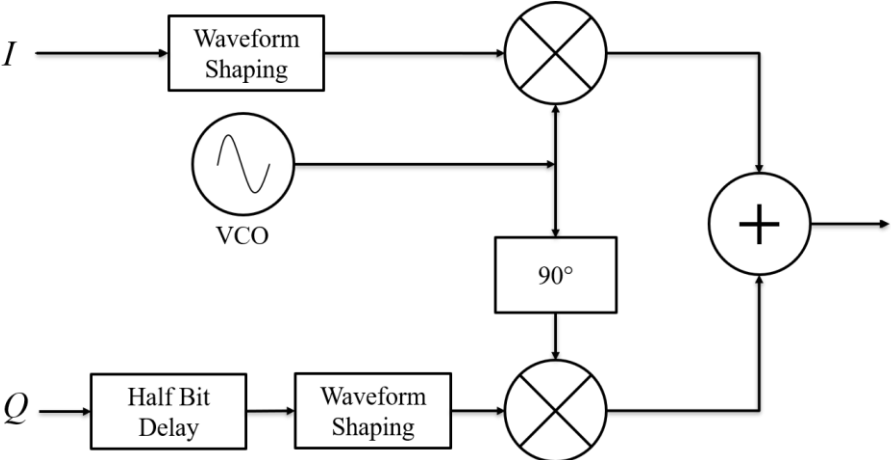


Figure 7. OQPSK modulation block diagram

Table 1. Current Deep Space Network Goldstone antenna downlink capabilities

	Frequency Ranges (MHz)	Gain (dBi)	Noise Temperature (K)
34 m BWG	S-band: 2200-2300	56.8	36.8
	X-band: 8400-8500	68.0	33.0
	Ka-band: 31800-32300	78.5	31.0
34 m HEF	S-band: 2200-2300	56.0	38.0
	X-band: 8400-85000	68.1	19.8
70 m	S-band: 2270-2300	63.4	22.0
	X-band: 8400-8500	74.4	20.6

### 3.4 Frequency Band Selection

The X-band is selected for CubeSat-earth communication to allow for compatibility with the DSN, which operates in the S, X, 26 GHz, and Ka bands [20]. The current capabilities of the DSN antennas at the Goldstone Deep Space Communications Complex are shown Table 1 [21]. The DSN provides several services for deep space communications. For command radiation or command delivery services, where the DSN transmits command data to the CubeSat, the DSN operates at S or X band using BPSK and PSK modulation with a maximum uplink data rate of 256 kbps and minimum of 7.8 bps. For telemetry, the S, X, and Ka bands are supported with PSK, BPSK, QPSK, or OQPSK modulation with a maximum downlink data rate of 10 Mbps (150 Mbps for near Earth Ka-band) and the minimum of 10 bps. The DSN also provides a beacon tone service to monitor the status of the CubeSat according to the transmitted beacon tones [22].

### 3.5 Link Budget

To further determine the requirements of the communication system for the CubeSat mission, a preliminary link budget is calculated for the X-band downlink. The performance of a communication link can be evaluated by the bit error rate (BER). Assuming an OQPSK modulation scheme, the signal-to-noise ratio (SNR) required to meet a received BER of  $10^{-4}$  is

8.4 dB [23]. The SNR indicates the degree to which the power of the received signal must surpass the power of the noise at the receiver to reliably interpret the modulated information.

The SNR is measured by the ratio  $E_b/N_0$ , where  $E_b$ , the energy per bit, is defined as

$$E_b = \frac{P_r}{R}, \quad (3.3)$$

where  $P_r$  is the power in Watts detected by the receiving antenna and  $R$  is the data rate in bits per second.  $N_0$ , the noise spectral density is defined as

$$N_0 = kT_s, \quad (3.4)$$

where  $k$  is the Boltzmann's constant in Joules/Kelvin and  $T_s$  is the system noise temperature which includes the antenna and receiver noise temperatures [24]. The  $T_s$  of DSN receivers are shown in Table 2 [25]. Using the known parameters of the receiving system, the required  $P_R$  to achieve the desired BER of  $10^{-4}$  can be calculated. The diplex X-band value of  $T_s$  is used for the calculations. For the minimum and maximum data rate capabilities of the DSN of 10 bps and 10 Mbps, the required received power is calculated to be -175.5 and -105.5 dBm, respectively, as shown in Table 3.

Table 2. System noise temperature of Deep Space Network antennas

Station	Operation	System Noise Temperature $T_s$
34 m BWG	Non diplex X-band	20.2 K
	Diplex X-band	29.2 K
70 m BWG	Non diplex X-band	20.2
	Diplex X-band	29.2

Table 3. Required received powers of Deep Space Network antenna for OQPSK

Parameter	$R = 10$ bps	$R = 10$ Mbps	Unit
BER	$10^{-5}$	$10^{-5}$	Magnitude (ratio)
SNR	8.4	8.4	dB
$P_r$	-175.5	-105.5	dBm

Table 4. Friis equation for downlink from CubeSat to earth

Input Parameters	Value	unit
$\lambda$	0.0355	m
$D$	40000000	m
$P_R$	-105	dBm
$P_T$	37	dBm
$G_R$	68	dBi
Output Parameters		
$G_t$	15	dBi

The maximum tolerable  $P_R$  at the DSN antenna is -90 dBm and the minimum detectable  $P_R$  is -172 dBm [25]. Therefore, the DSN receivers can fulfill the requirements for OQPSK modulation from 10 bps to 10 Mbps. Next, the required received power at the ground station receivers is used to determine the required specifications of the CubeSat transmitting system. To achieve  $P_R$  at the ground station, the transmitting system must overcome significant free space loss. To determine the antenna gain and power of the link, the Friis equation is used, as given by [26]

$$P_R = P_T + G_T + G_R + 20 \log \left( \frac{\lambda}{4\pi D} \right), \quad (3.5)$$

where  $P_T$  is the transmitted power,  $G_T$  is the transmit antenna gain,  $G_R$  is the receive antenna gain,  $\lambda$  is the wavelength of the transmit center frequency, and  $D$  is the distance between the CubeSat and the earth. The values used for the Friis equation are shown in Table 4. With the

known  $G_R$  and  $P_R$  of the DSN antennas, and estimated  $P_T$  of 5 W based on the Iris radio, the required  $G_T$  is calculated to be 15 dBi at 8.45 GHz.

Additional losses must be accounted for in a satellite link budget. Atmospheric attenuation occurs when signals passing through the earth's atmosphere are attenuated by absorption, scattering, and reflections from particles. Additionally, transmission through the earth's ionosphere suffers from losses caused by electrons and cations. Rain and weather attenuation are especially important for higher frequency bands. Pointing losses for a parabolic antenna are estimated at 0 to 1 dB due to loss of alignment between the transmitting and receiving antennas. Additionally, a loss of 4-6 dB is expected to occur due to the interference caused by sun's wideband electromagnetic waves reflecting on the moon's surface (lunar flux density loss) [27]. A complete link budget should account for additional losses and plan for a link margin.

### **3.6 Bandwidth**

The bandwidth required for CubeSat to DSN communication must be considered. The chosen modulation scheme, OQPSK, has a bandwidth efficiency of 2 bps/Hz. With the maximum data rate of the DSN being 10 Mbps, the CubeSat system must operate with at least 5 MHz of bandwidth. However, to increase the capabilities of deep space data collection, industry is pushing to develop deep space communication at higher rates. NASA is proposing a Space Communication Rates At Multi-Gbps (SCRAM) technology to increase the communication capabilities for sensors such as synthetic aperture radar [28]. SCRAM proposes a lunar communication link in the Ka-band with data rate capabilities from 100 Mbps to 2.2 Gbps. Data rates of 2.2 Gbps will require at least 1.1 GHz of bandwidth. To address the increasing

requirements of data rate and possible expansion of the DSN, this system is designed for a bandwidth higher than 1.0 GHz to enable data rates of 2.0 Gbps.

## CHAPTER 4: ANTENNA DESIGN

### 4.1 Antenna Characteristics

The design of an antenna for CubeSat applications must address the standard requirements of satellite antennas in addition to limitations on power and size. The link budget analysis determined that an antenna array with high gain ( $> 15$  dBi) and wide bandwidth ( $> 1.0$  GHz) is required. Regarding size requirements for the 6U, the planar MGA must require less than 1U of volume (10 cm x 10 cm x 10 cm) and less than 20 cm x 60 cm of surface area.

Satellite antennas are also required to be circularly polarized to maximize power transfer. A linearly polarized antenna suffers from dependency on antenna orientation, with up to 3.0 dB loss caused by polarization mismatch. Even in the case of a highly accurate pointing and alignment mechanism, waves traveling through the ionosphere are affected by the Faraday effect: free electrons cause variable rotation of waves in the ionosphere depending on the electron density. Additionally, as CubeSats do not use pointing mechanisms and are limited in propulsion ability, the desired antenna has wide circular polarization and half-power beam width (HPBW) greater than  $50^\circ$  to allow for more opportunities of line-of-sight communication.

Spiral antennas fulfill the requirements for wideband operation, circular polarization, and minimal volume. The spiral antenna has broadband performance because it is a type of frequency independent antenna. Frequency independent antennas were first introduced as broadband antennas that utilize a geometry only determined by angles, allowing for performance to be independent of wavelength and theoretically able to operate at any frequency [26]. In practice, independent frequency antennas have limited bandwidth dependent on the size and feed of the

antenna. Spiral antennas, first proposed in the 1950s, include structures such as the equiangular spiral [29] [30], logarithmic spiral [30], and Archimedean spiral [31]. The Archimedean is not completely determined by angles, but still has comparable bandwidth and performance to the angle-determined logarithmic and equiangular spiral. The antenna design does have better axial ratio at lower frequencies compared to the equiangular [32]. For this thesis, a two-arm Archimedean spiral antenna was chosen as the base for the antenna array design.

## 4.2 Archimedean Spiral

### 4.2.1 Theory of Operation

The two-arm Archimedean spiral antenna (ASA) was first proposed by J. Kaiser in 1960 [31]. The geometry utilizes the Archimedean spiral, which can be described in polar coordinates  $(r, \theta)$  by the following equation:

$$r = a + b\theta \quad (4.1)$$

where  $a$  is a real number that offsets the start of the spiral from the origin and  $b$  is a real number that controls the separation between the spiral loops. As shown in Figure 8, the ASA can be easily generated using this equation.

Although the spiral is composed of two transmission lines, the geometry of the spiral transforms it into a radiating structure [29]. The two-arm spiral has a balanced feed at the center, where one arm is fed with a current  $180^\circ$  out-of-phase from the other. Radiation at a specific frequency occurs when the circumference of the spiral, or “ring” is equivalent to one wavelength. Therefore, the maximum circumference of the spiral limits the upper operating frequency. The “ring theory,” agrees well with experimental observations [33]. As shown in Figure 9, radiation

at 3.0 GHz shows higher surface current on the outer rings as compared to radiation at the lower frequency of 12 GHz.

The resulting radiation from the ASA is two broad beams, one normal to each side of the spiral, with right-hand circular polarization on one side and left-hand circular polarization on the opposite side. If back-lobe radiation is undesired, a backing cavity or absorber can be used. The ASA can be difficult to match for feeding purposes as the theoretical impedance of a spiral

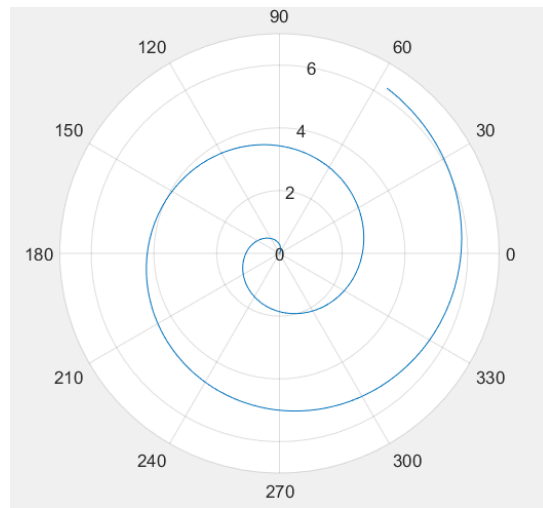


Figure 8. Archimedean spiral generated in MATLAB with  $a = 1$  and  $b = 2$  for  $\theta = 0$  to  $2\pi$

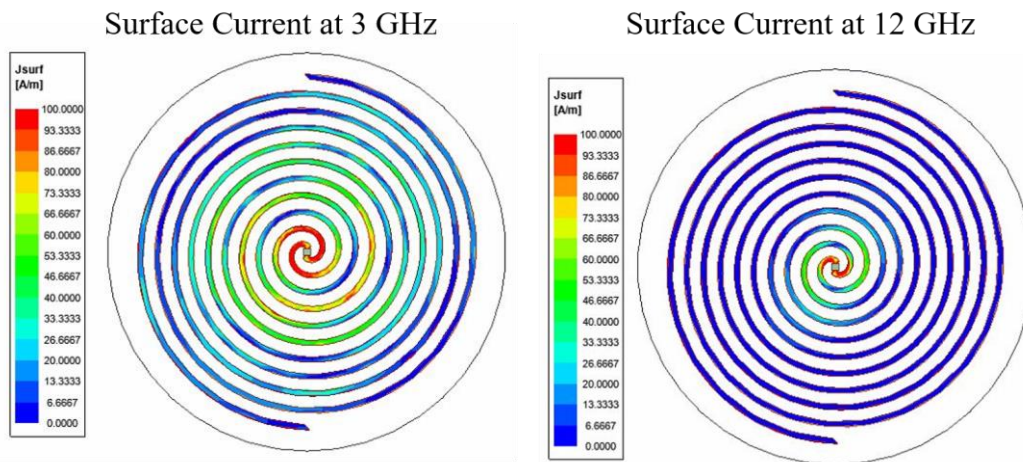


Figure 9. Surface current distribution of two-arm Archimedean spiral antenna

antenna is 188.5 Ohms. The theoretical impedance is derived from Babinet's principle.

Originally applied to optics, Babinet's principle considers a field placed behind a screen that has an opening. When this field is added to the field of a complimentary structure, the sum of the two fields is equal to the field when there is no screen. A complimentary structure is opaque where the original structure is transparent and is transparent where the original structure is opaque.

When applied to antennas, the principle states that in a medium with intrinsic impedance,  $\eta$ , two complimentary structures with terminal impedances of  $Z_s$  and  $Z_c$ , are related by [26]

$$Z_s Z_c = \frac{\eta^2}{4} \quad (4.2)$$

If a two-arm spiral is rotated by  $90^\circ$ , the rotated structure will form the compliment; therefore, a two-arm spiral antenna is self-complimentary ( $Z_s = Z_c$ ). In free space, the theoretical impedance of a two-arm spiral antenna is  $188.5 \Omega$ , regardless of the spiral type, arm spacing and size, or number of turns. In practice, the impedance ranges from 150 to 170 Ohms, with differences being caused by feeding mechanism and arm trace width variations [26].

#### 4.2.2 Design

Using ANSYS High Frequency Structure Simulator (HFSS v. 17.2), an ASA was designed as shown in Figure 10 for a minimum operating frequency of 3.0 GHz. Two radiator

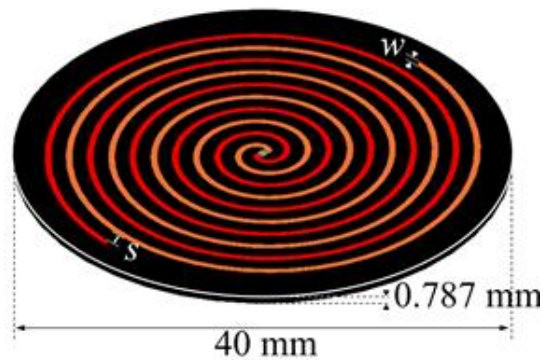


Figure 10. The two-arm Archimedean spiral antenna

arms (number of turns ( $n$ ): 5, radiator width ( $w$ ): 0.7 mm, spacing ( $s$ ): 1.0 mm) are placed on a Rogers RT/duroid 5880 substrate, which has a diameter of 40 mm, a thickness of 0.787 mm, and a relative dielectric constant ( $\epsilon_r$ ) of 2.2. The simulation uses a lumped port with port impedance of 170 Ohms.

The optimized ASA performance shows good impedance matching with wide gain bandwidth, as the reflection coefficient,  $|\Gamma|$ , is lower than -10 dB for frequencies above 3.0 GHz. Wide circular polarization bandwidth is achieved as the axial ratio at boresight ( $AR_{00}$ ) is lower than 3.0 dB at frequencies from 3.5 to 33.8 GHz (full range not shown). At 8.45 GHz, the spiral has a HPBW of  $70^\circ$  and axial ratio beam width (ARBW) of  $80^\circ$ , as shown in Figure 11. As shown in Figure 12, the realized gains at boresight ( $RG_{00}$ ) are 5.6 dBi at 8.45 GHz and 7.0 dBi at 12 GHz. The radiation efficiency of the ASA is  $> 99.8\%$  at frequencies above 8 GHz.

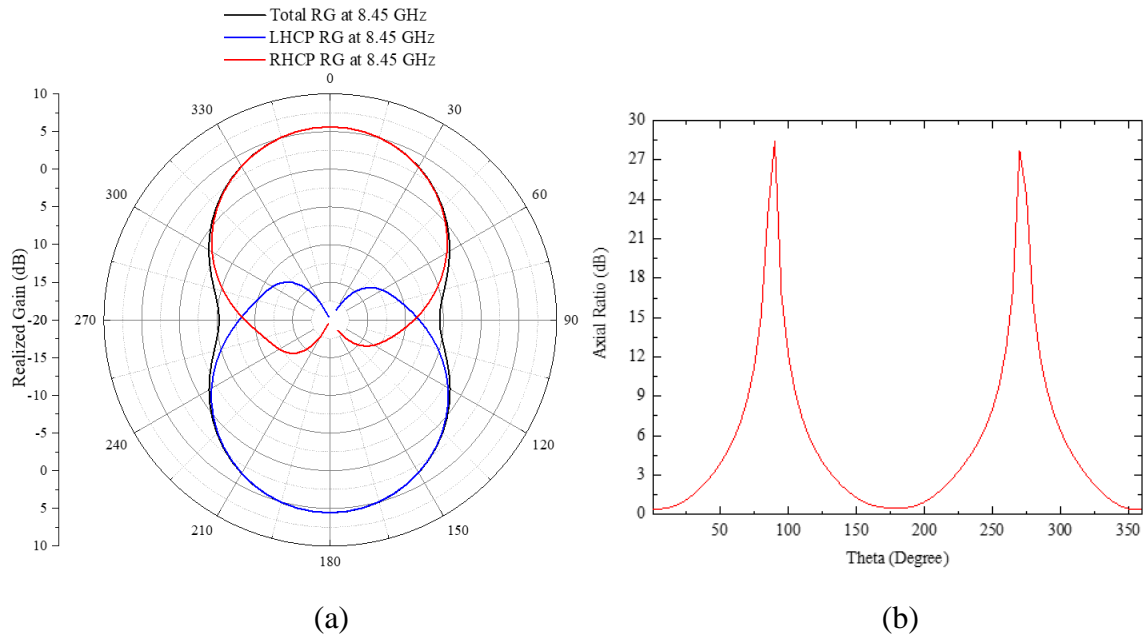


Figure 11. The (a) radiation pattern and (b) axial ratio pattern of the two-arm Archimedean spiral antenna at 8.45 GHz

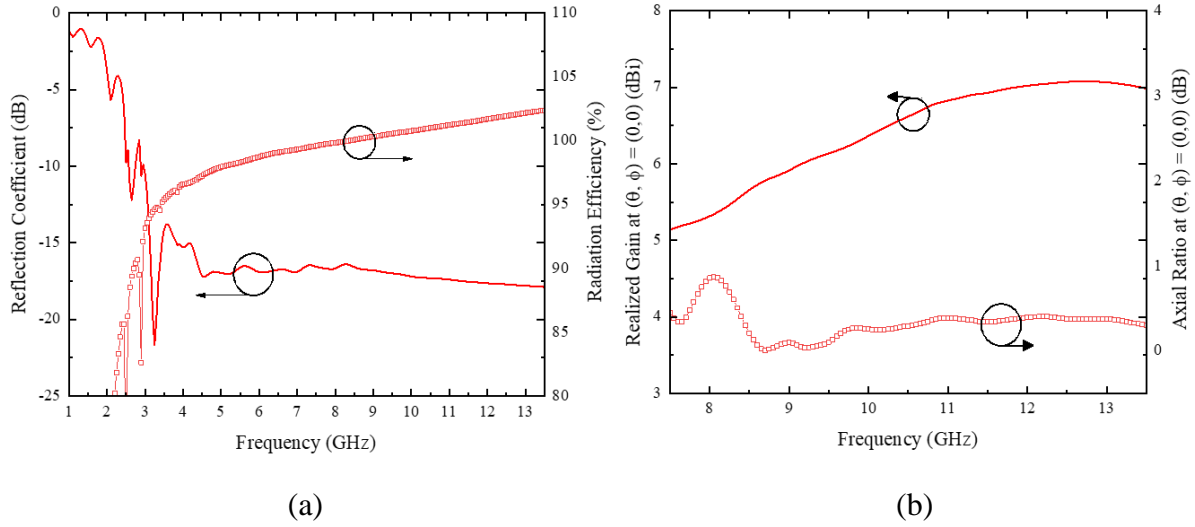


Figure 12. The (a) reflection coefficient and radiation efficiency and (b) realized gain and axial ratio as a function of frequency of the two-arm Archimedean spiral antenna

### 4.3 Microstrip Balun

#### 4.3.1 Theory of Operation

Feeding of the ASA poses two problems: (i) the impedance of the ASA is not 50 ohms and (ii) two balanced conductors are required to feed the antenna. Because of this, the ASA will require modification to allow connection to a standard SMA cable. To address issue (i), transformation of an impedance to feed an antenna can be achieved using a quarter-wave microstrip impedance transformer, where the impedance of a matching transmission line of quarter-wave length is determined by [34]

$$Z_1 = \sqrt{Z_0 R_L} \quad (4.3)$$

where  $Z_1$  is the impedance of the matching section,  $Z_0$  is the initial impedance, and  $R_L$  is the load impedance. The performance can be evaluated using the absolute value of the reflection coefficient,  $|\Gamma|$ , which is

$$|\Gamma| = \left| \frac{Z_{in} - Z_0}{Z_{in} + Z_0} \right|, \quad (4.4)$$

where  $Z_{in}$  is the input impedance looking into the matching section, defined as

$$Z_{in} = Z_1 \frac{Z_L + jZ_1 \tan \beta \ell}{Z_1 + jZ_L \tan \beta \ell}, \quad (4.5)$$

where  $\theta = \beta \ell$ . The  $\beta$  is the phase constant and  $\ell$  is the length of the transmission line, so the transformer is frequency dependent. For the quarter wave transformer,  $|\Gamma|$  can be approximated as

$$|\Gamma| = \frac{|Z_L - Z_0|}{2\sqrt{Z_0 Z_1}} |\cos \theta| \quad \text{for } \theta \text{ near } \pi/2. \quad (4.6)$$

To increase the bandwidth of the transformer, sequential matching sections can be added. An impedance taper can be achieved when the amount of matching sections approaches infinity. To address issue (ii), the modal or unbalanced-balanced transformation can likewise be achieved by tapering an unbalanced microstrip transmission line to a balanced parallel stripline.

### 4.3.2 Design

For this system, the balun is desired to operate from 8.0 to 12 GHz and transform the impedance from 50 Ohm to 170 Ohm with minimal space consumption. First, the impedance transformation will be discussed, followed by the impedance and modal transformation. For comparison, three different impedance taper profiles are used in the design of the impedance transformer: (i) linear, (ii) exponential, and (iii) Klopfenstein, as shown in Figure 13. All impedance transforming baluns will have a length ( $L_B$ ) of 40 mm, with 50 divisions ( $d$ ) along the length where the impedance and width are calculated. The tapers have an initial impedance ( $Z_0$ ) of 50 Ohm and final impedance ( $Z_L$ ) of 170 Ohm.

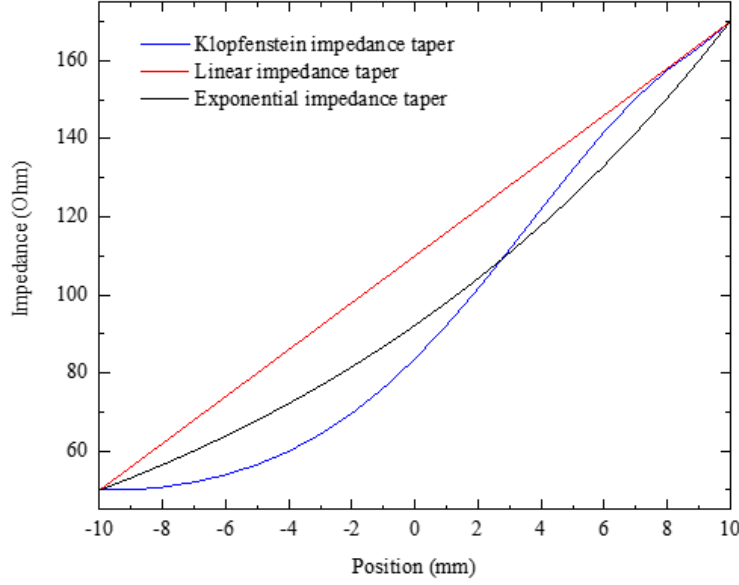


Figure 13. Impedance tapers for transition from 50 to 170  $\Omega$

The linear impedance taper is calculated as a function of the length,  $z$ :

$$Z(z) = Z_0 + (Z_L - Z_0) \frac{z}{L} \quad (4.7)$$

where  $l$  is the set of  $d$  numbers between 0 and  $L$ .

The exponential transform was also designed according to following equations:

$$Z(z) = Z_0 e^{az} \quad (4.8)$$

$$a = \frac{1}{L} \ln \left( \frac{Z_L}{Z_0} \right) \quad (4.9)$$

The Klopfenstein transform was developed to minimize  $|\Gamma|$  of the impedance transformation via the impedance step given by [35]

$$\ln Z(z) = \frac{1}{2} \ln Z_0 Z_L + \frac{\Gamma_0}{\cosh A} A^2 \phi \left( \frac{2z}{L} - 1, A \right) \quad \text{for } 0 \leq z \leq L, \quad (4.10)$$

where the function  $\phi(x, A)$  is defined by

$$\phi(x, A) = -\phi(-x, A) = \int_0^x \frac{I_1(A\sqrt{1-y^2})}{A\sqrt{1-y^2}} dy \quad \text{for } |x| \leq 1, \quad (4.11)$$

where  $I_1(x)$  is the modified Bessel function and  $\phi(x, A)$  must be calculated numerically, but has the special values

$$\phi(0, A) = 0, \quad (4.12)$$

$$\phi(x, 0) = \frac{x}{2}, \quad \text{and} \quad (4.13)$$

$$\phi(1, A) = \frac{\cosh A - 1}{A^2}. \quad (4.14)$$

The  $\Gamma$  of this impedance transformation is given by

$$\Gamma(\theta) = \Gamma_0 e^{-j\beta L \frac{\cos\sqrt{(\beta L)^2 - A^2}}{\cosh A}} \quad \text{for } \beta L > A, \quad (4.15)$$

where  $\Gamma_0$  is the reflection coefficient at zero frequency, defined as

$$\Gamma_0 \cong \frac{1}{2} \ln\left(\frac{Z_L}{Z_0}\right). \quad (4.16)$$

The passband of the taper occurs when  $\beta L > A$ , where  $|\Gamma|$  will have a maximum ripple of

$$\Gamma_m = \frac{\Gamma_0}{\cosh A}. \quad (4.17)$$

To minimize variation in the reflection coefficient in the passband,  $\cosh A$  is selected to have a value of 20, to allow for the maximum ripple to be one-twentieth of  $\Gamma_0$ .

To address the discontinuities of the Klopfenstein taper at the initial and final impedance steps, Hecken modified the impedance profile to [36]

$$\ln Z(z) = \frac{1}{2} \ln Z_0 Z_L + \frac{1}{2} \ln\left(\frac{Z_L}{Z_0}\right) \phi\left(A, \frac{2z}{L}\right) \quad \text{for } 0 \leq z \leq L, \quad (4.18)$$

where the function  $\phi(A, \eta)$  is defined by

$$\phi(A, \eta) = \frac{A}{\sinh A} \int_0^\eta I_0(A\sqrt{1-u^2}) du \quad (4.19)$$

where  $A$  is chosen with the same method used for the Klopfenstein taper.

The taper is implemented using a microstrip transmission line. The impedance of a microstrip can be calculated using the following equations [34]

$$Z_0 = \begin{cases} \frac{60}{\sqrt{\epsilon_e}} \ln \left( \frac{8d}{W} + \frac{W}{4d} \right) & \text{for } W/d \leq 1 \\ \frac{120\pi}{\sqrt{\epsilon_e} [W/d + 1.393 + 0.667 \ln(W/d + 1.444)]} & \text{for } W/d \geq 1 \end{cases}, \quad (4.20)$$

where  $W$  is the width of the microstrip line,  $d$  is the height of the dielectric, and  $\epsilon_e$  is the effective dielectric constant given by

$$\epsilon_e = \frac{\epsilon_r + 1}{2} + \frac{\epsilon_r - 1}{2} \frac{1}{\sqrt{1 + 12d/W}}, \quad (4.21)$$

$\epsilon_r$  is the relative permittivity. Using these equations, the linear, exponential, and Klopfenstein tapered microstrips were designed to transform the impedance from 50 to 170 Ohms as shown in Figure 14. The resulting impedance transforms were simulated in HFSS and the results are shown in Figure 15. As expected, the Klopfenstein taper shows the lowest maximum  $|\Gamma|$  compared to the linear and exponential of same length and material. One disadvantage of the Klopfenstein is the increase to the lower limit to the passband.

The microstrip transformer can be modified to transform from the unbalanced microstrip to the balanced parallel stripline by tapering the ground plane. In this case, the microstrip impedance equation cannot be applied to the transition section or stripline. Therefore, the width of the signal and ground conducting layers are calculated using the process outlined in [37] [38].

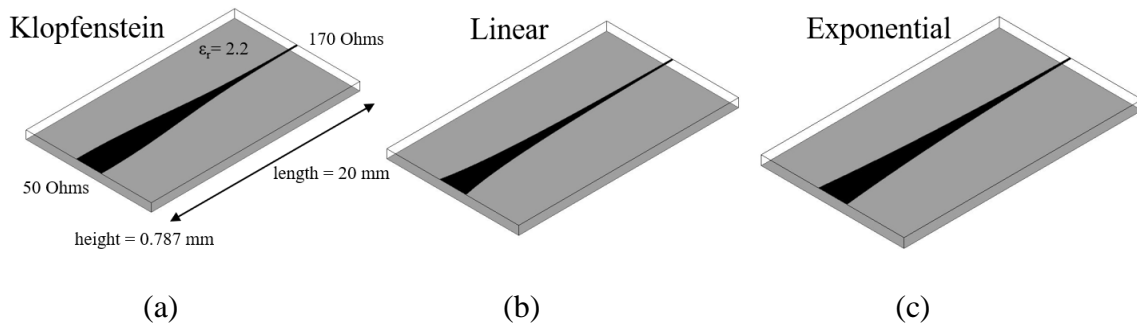


Figure 14. Microstrip impedance transformers: (a) Klopfenstein, (b) linear, and (c) exponential tapers

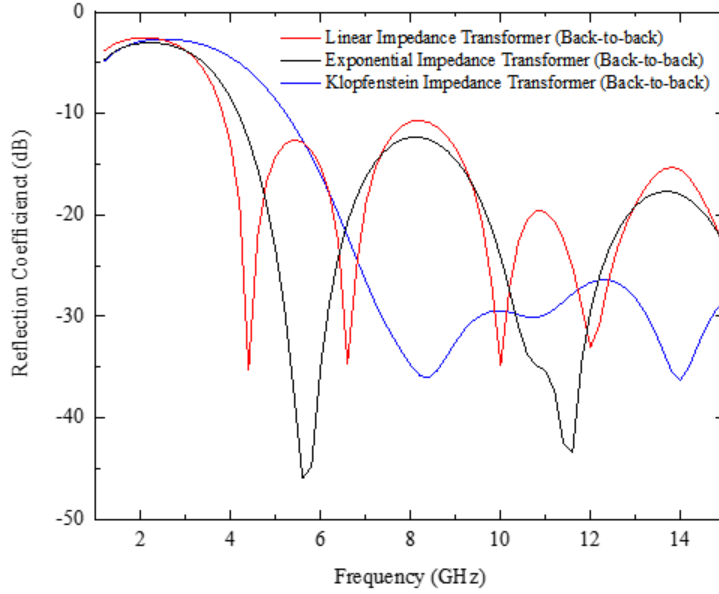


Figure 15. Simulated reflection coefficient of microstrip impedance tapers

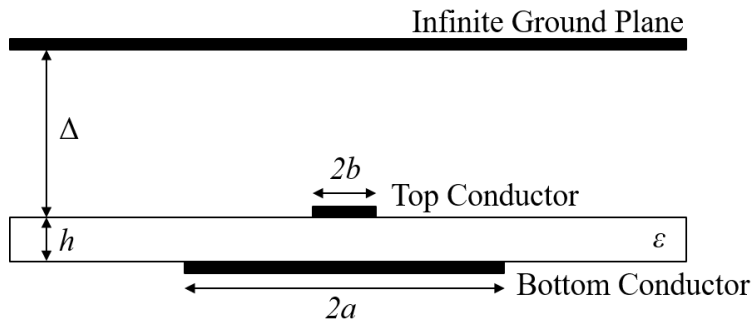


Figure 16. Transversal cut of asymmetrical double-sided strip lines

A conformal mapping technique [37] is applied to determine the impedance of the quasi-TEM operation of asymmetrical double-sided strip lines, as shown in Figure 16. The impedance is determined to be

$$Z_0 = \frac{60\pi}{\sqrt{\epsilon_e} \left( \frac{K(v)}{K(\alpha)} + \frac{K(\alpha')}{K(v')} \right)}, \quad (4.22)$$

where  $\epsilon_e$  is the effective dielectric constant given by

$$\epsilon_e = \frac{C}{C_0} = \frac{\frac{K(v') + \epsilon_r \frac{K(\alpha')}{K(\alpha)}}{\frac{K(v) + K(\alpha)}{K(v) + K(\alpha)}}}{\frac{K(v) + K(\alpha)}{K(v) + K(\alpha)}} \quad (4.23)$$

$K(\lambda)$  is the complete elliptical integral given by

$$K(\lambda) = \int_0^{\pi/2} \frac{dx}{\sqrt{1 - \lambda^2 \sin^2 x}} \quad (4.24)$$

and

$$v = \operatorname{sech} \left( \frac{\pi b}{2\Delta} \right), \quad v' = \sqrt{1 - v^2}, \quad (4.25) \quad (4.26)$$

$$\alpha = \sqrt{\frac{2(x_a + x_b)}{(1 + x_b)(1 + x_a)}}, \quad \alpha' = \sqrt{1 - \alpha^2}, \quad (4.27) \quad (4.28)$$

$$x_a = \cosh \left( \frac{a\pi}{h} \right) \quad \text{and} \quad x_b = \cosh \left( \frac{b\pi}{h} \right) \quad (4.29) \quad (4.30)$$

where  $\Delta$  is chosen to be approximately  $20h$ .

Thus, the asymmetrical doubled-sided strip line is applied to the Klopfenstein taper for impedance matching. First, the top layer is designed to be a direct linear geometric taper from the microstrip width at 50 Ohm to the stripline width at 170 Ohms, where both widths are calculated using the impedance method described. Then, using the tapering method described for the impedance transformer, the width of the bottom layer is calculated for the Klopfenstein impedance taper profile. Klopfenstein was chosen due to the lowest  $\Gamma_0$  in the passband. The designed baluns were simulated HFSS as back-to-back transitions, as shown in Figure 18. The Klopfenstein taper [35] was chosen for the final design with a length of 40 mm, which corresponds to a 0.925 wavelength of the lowest operating frequency at 8 GHz.

To verify the mode transformation, a parallel stripline with length of 20 mm is inserted between two baluns, as shown as an inset in Figure 20, to ensure the parallel stripline mode is achieved. As shown in Figure 20, the S-parameters are not significantly changed by the 20 mm parallel stripline and the passband from 3.0 to 10 GHz is maintained.

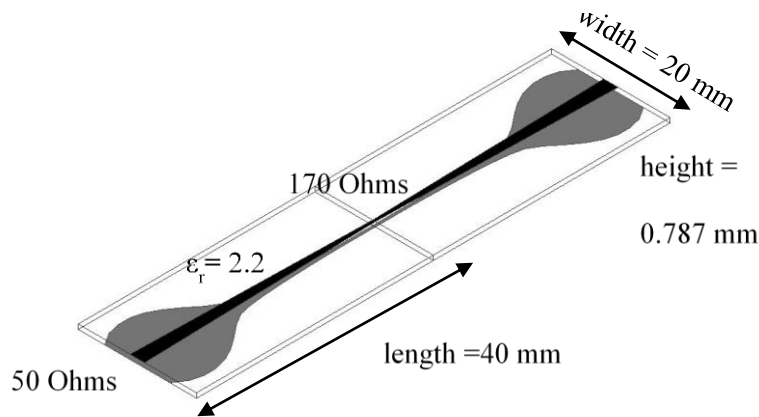


Figure 17. Designed back-to-back Klopfenstein balun on Rogers RT/duroid 5880

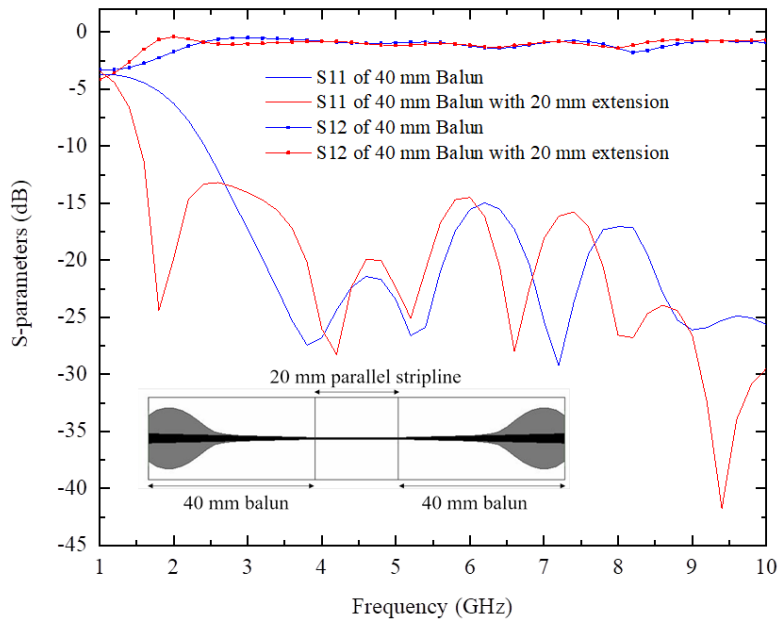


Figure 19. Reflection coefficient of Klopfenstein balun with 20 mm parallel stripline extension

### 4.3.3 Fabrication and Measurement

To characterize the performance of the microstrip transitions, they were fabricated in a back-to-back configuration, as shown in Figure 22. This configuration allows for the microstrips to be evaluated using SMA connectors on the microstrip sections. As shown below, a microstrip impedance transformer with a length of 20 mm was fabricated on Rogers RT/duroid 5880 using

a milling machine. The S-parameters of the 2-port network were measured using an Agilent Vector Network Analyzer (VNA) N5230A, as shown in Figure 24. The simulated and measured results are shown in Figure 26. The measured passband occurs from 5.0 to 10 GHz ( $|\Gamma| < -10$  dB) with an insertion loss,  $|S_{12}|$ , of  $< 2.6$  dB. Discrepancies between expected and measured results are due to fabrication error and low conductivity of the solder connections.



Figure 21. Fabricated back-to-back microstrip impedance transformer on Rogers RT/duroid 5880

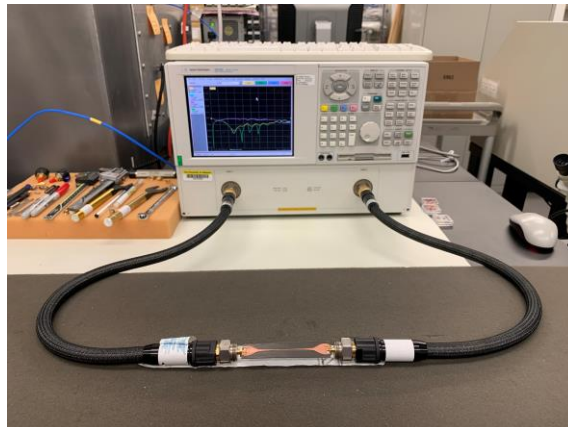


Figure 23. Measurement setup of S-parameters using Agilent Vector Network Analyzer N5230A

Next, the 40 mm Klopfenstein balun was fabricated, as shown in Figure 28. The measured and simulated results are shown in Figure 30. The measured passband occurs from 2.5 to 10 GHz ( $|\Gamma| < -10$  dB) with an insertion loss of  $< 1.8$  dB, suitable for feeding the ASA.

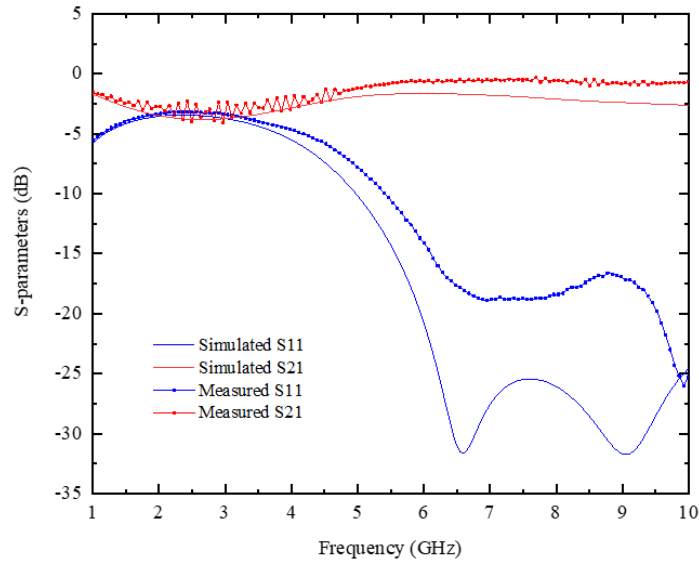


Figure 25. Measured and simulated S-parameters of back-to-back microstrip impedance transformer ( $L = 20$  mm, Klopfenstein taper, Rogers RT/duroid 5880)



Figure 27. Fabricated back-to-back Klopfenstein balun

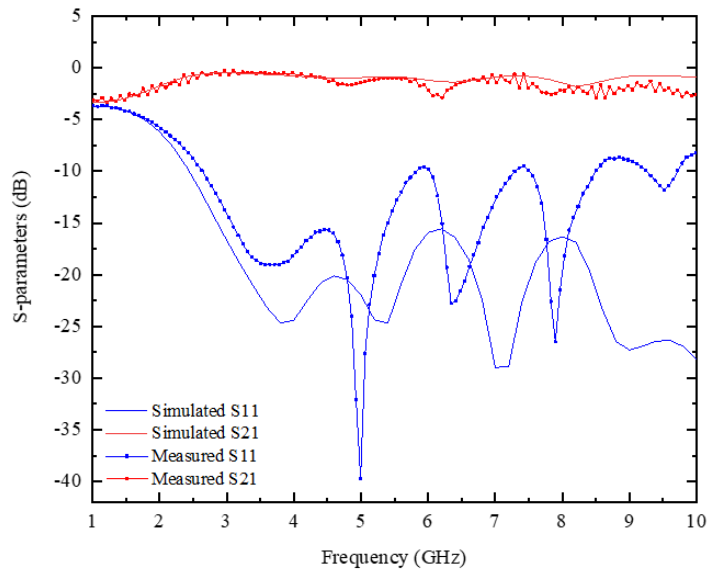


Figure 29. Measured and simulated S-parameters of back-to-back Klopfenstein balun

## 4.4 Backing Cavity

### 4.4.1 Theory of Operation

As explained in section 4.2.1, the ASA radiates in two opposite directions. For CubeSat applications, the back-lobe radiation may cause unwanted interference with the CubeSat's electronic systems. An absorbing material or backing cavity should be added to the antenna structure. The absorbing material can protect the CubeSat from undesired radiation but allows half of the antenna's radiating power to be wasted. A backing cavity will reflect the back-lobe radiation. The back-lobe waveform will constructively interfere with the front lobe and increase the antenna gain. However, the cavity limits the impedance and axial ratio bandwidth of the antenna.

#### 4.4.2 Design

To investigate this behavior, the ASA is backed by a conventional backing cavity (CBC) with a height of  $h$  and simulated in HFSS. As shown in Figure 32, the copper cavity has a wall thickness of 1.5875 mm and diameter of 40 mm. A parametric study is performed on  $h$  regarding the effect on  $RG_{00}$  and  $AR_{00}$ , as shown in Figure 34 and Figure 36, respectively. The  $h$  is evaluated at values from 2.0 mm to 20 mm in steps of 2.0 mm. By increasing  $h$ , the impedance and  $AR_{00}$  bandwidths were increased. It can be observed from the simulated data that to maintain the  $AR_{00}$  and impedance lower frequency limits,  $h$  must be 6.0 mm or larger. Notably, the  $RG_{00}$  and  $AR_{00}$  show high fluctuations at the center of the frequency bands at several cavity heights.

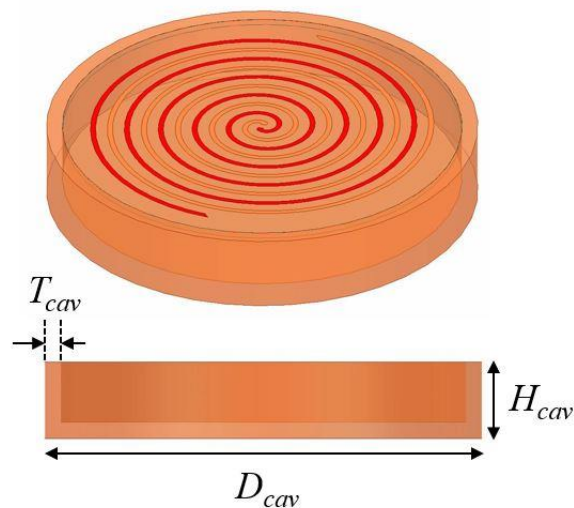


Figure 31. Backing cavity for Archimedean spiral antenna

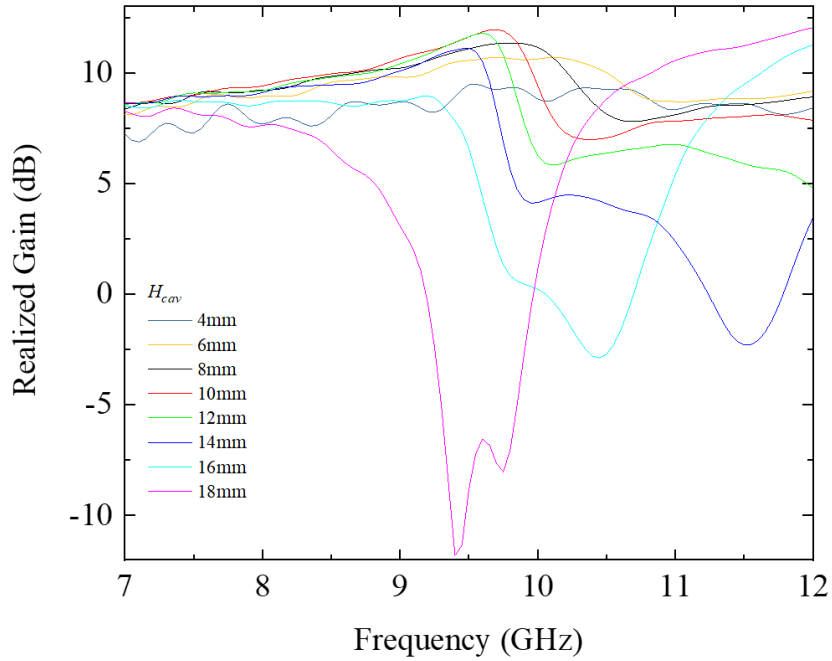


Figure 33. Effect of cavity height on realized gain at boresight of Archimedian spiral antenna

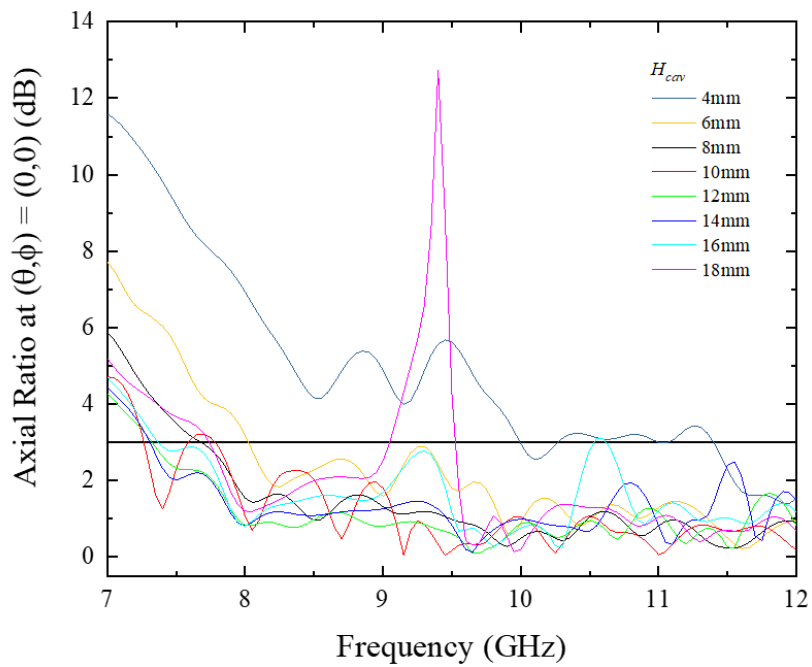


Figure 35. Effect of cavity height on axial ratio at boresight of Archimedian spiral antenna

To maximize gain,  $h$  should be one quarter wavelength at the intended frequency [33]. In this case, to maximize gain at 8.0 GHz,  $h$  should be approximately 9.3 mm, and to maximize

gain at 12 GHz,  $h$  should be approximately 6.25 mm. A cavity with a single height cannot be optimized for gain at all frequencies. The cavity height, when optimized for one frequency, causes a decrease in  $RG_{00}$  at higher frequencies. The frequency corresponding to the cavity height of a half wavelength is the most affected, as shown in Figure 25. From the parametric study, the  $h$  of 8.0 mm provides a low  $RG_{00}$  ripple in the frequency range of interest and maintains the desired  $AR_{00}$  bandwidth. Therefore, the 8.0 mm CBC will be further investigated.

To achieve a broadband solution, the effect of cavity geometry on antenna performance was further investigated. Utilizing the “ring theory” that states the spiral radiates from circumferential “rings” dependent on the operating frequency, the height of the cavity was varied as a function of distance from the center of the cavity. As a result, a sloped-wall backing cavity (SWBC) was designed to optimize gain, as shown in Figure 38. An  $H_{cav}$  of 8.0 mm was chosen for the design to maintain the AR bandwidth from 8.0 to 12 GHz. From a parametric sweep of lower radius from 5.0 mm to 15 mm (step of 2.5 mm), lower radiuses below 12.5 mm have enough AR bandwidth. A radius below 15 mm can achieve high  $RG_{00}$  and remove the drop from 8.0 to 12 GHz.

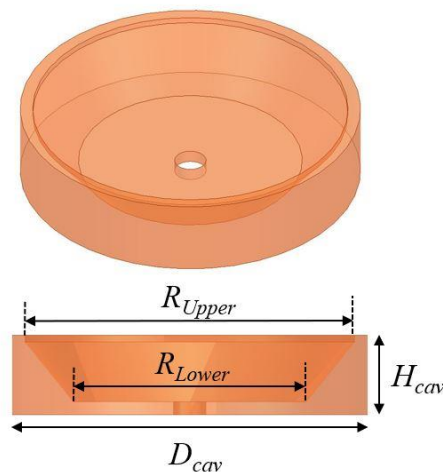


Figure 37. Sloped wall backing cavity for Archimedean spiral antenna

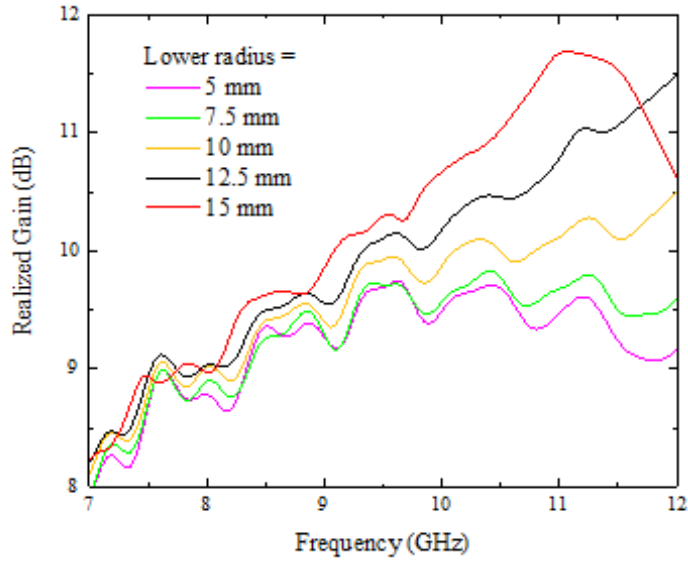


Figure 39. Effect of lower radius of sloped wall backing cavity on realized gain at boresight of the Archimedean spiral antenna

The optimized SWBC has a  $H_{cav}$  of 8.0 mm, lower radius ( $R_{lower}$ ) of 14.2 mm, and upper radius ( $R_{upper}$ ) of 20 mm. The SWBC is found to increase  $RG_{00}$  of the ASA by 3.6 to 4.8 dBi from 8.0 to 12 GHz, as shown in Figure 40. Above 13 GHz,  $RG_{00}$  of both SWBC and CBC decrease due to destructive interference from reflected waves. The cavity maintains the desired beamwidth at 8.45 GHz: the HPBW is  $68^\circ$  and the ARBW is  $55^\circ$ . The SWBC, which contains the same volume as the CBC, provides less gain fluctuation in comparison to the CBC, Figure 29. The SWBC has a lower AR bandwidth compared to the CBC, but still achieves  $< 3.0$  dB from 8.0 to 12 GHz.

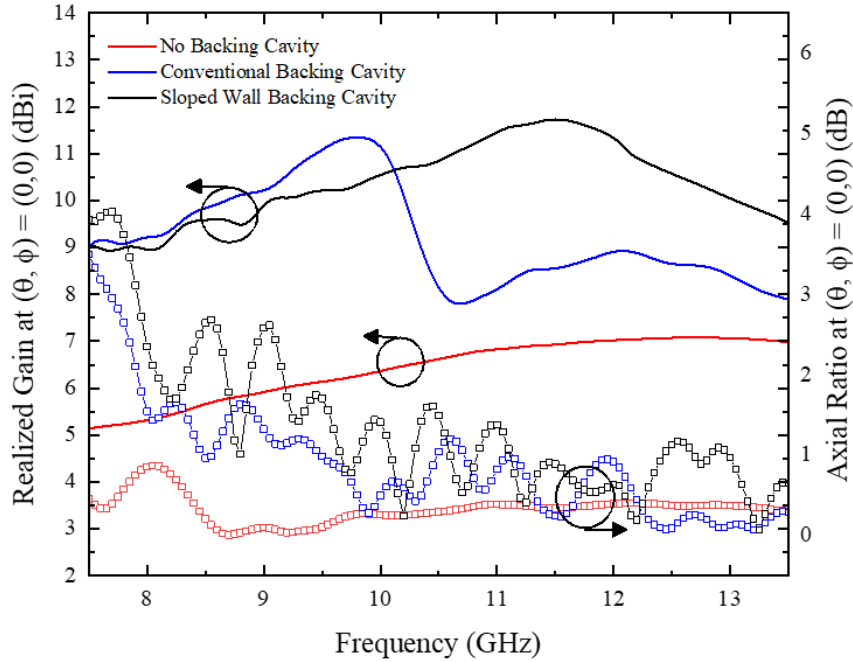


Figure 41. Realized gain and axial ratio at boresight of Archimedean spirals antennas with (i) no backing cavity, (ii) conventional backing cavity with 6 mm height, and (iii) sloped wall backing cavity

## 4.5 Spiral Array

### 4.5.1 Design

The high gain required for deep space communication is achieved with an antenna array designed to utilize the SWBC-ASA. First, a 4 x 4 planar array is designed for the 1U face (100 mm x 100 mm) of a 3U CubeSat, as shown in Figure 44.

With a distance  $d_{array}$  between elements of 10 mm, the 4 x 4 ASA array and 4 x 4 SWBC-ASA array were simulated and compared. Like previously, the ASA array suffers from a large drop in  $RG_{00}$  ( $> 4.0$  dBi) from 10 to 10.5 GHz and increases the  $RG_{00}$  of the ASA array by  $< 2.0$  dBi from 10.5 to 12 GHz, as shown in Figure 46. To address this problem, the SWBC-ASA array was optimized. The  $R_{lower}$  was optimized to 13 mm for high  $RG_{00}$  and low  $AR_{00}$  from 8.0 to 12 GHz. The SWBC-ASA array shows a 3.2 to 4.8 dBi increase of the  $RG_{00}$  of the ASA array. The

SWBC-ASA array shows low gain variation in comparison to CBC and maintains the desired AR bandwidth. The radiation pattern, not pictured, has a HPBW of  $20^\circ$ . The HPBW can be improved if spacing between array elements increases.

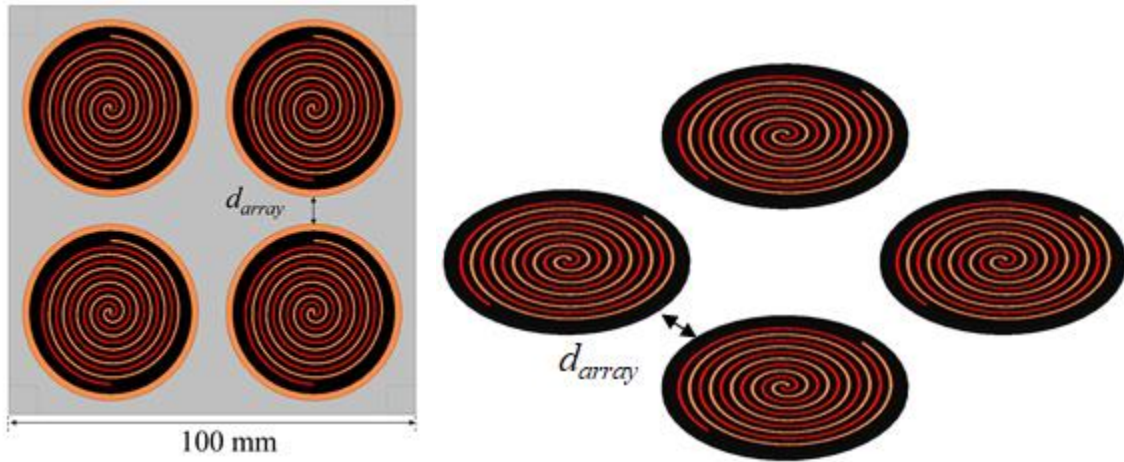


Figure 43. The 4 x 4 Archimedean spiral antenna array on 1U CubeSat face (100 cm x 100 cm)

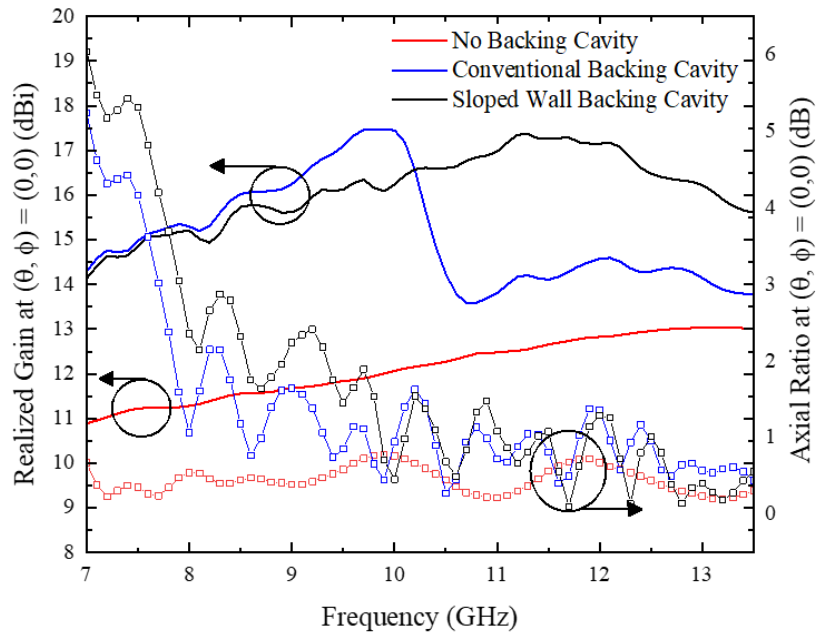


Figure 45. Realized gain and axial ratio at boresight of 4 x 4 Archimedean spiral antenna array with (i) no backing cavity, (ii) conventional backing cavity and (iii) sloped wall backing cavity

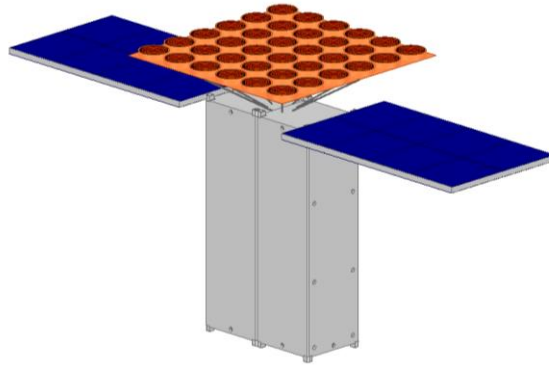


Figure 47. Proposed deployable sloped wall cavity-backed Archimedean antenna array

#### **4.5.2 Proposed 6x6 Spiral Array**

The designed SWBC-ASA Array achieves a  $RG_{00}$  of 17 dBi at 11 GHz with 4 ASA elements. To increase link margin for the lunar CubeSat or apply the designed system to farther destinations in deep space, such as Mars, a higher gain is desired. To achieve this, a deployable SWBC-ASA Array, as shown in Figure 48, is proposed to achieve a  $RG_{00}$  of 27 dBi at 11 GHz with 36 ASA elements.

#### **4.6 Power Splitter**

##### **4.6.1 Theory of Operation**

To feed the 4 x 4 antenna arrays, a power splitter was required to allow the array to be fed from a single source. A Wilkinson power splitter was chosen due to its ease in design and isolation between output ports. The Wilkinson power splitter is a three-port system, where the two output ports, Port 2 and 3, are connected by a resistor to ensure isolation and matching of the ports. The configuration shown in Figure 50 can be easily implemented with a microstrip transmission line, where the power splitter utilizes the quarter wavelength impedance transformer.

### 4.6.2 Design

Using HFSS, a power splitter was designed and simulated, as shown in Figure 52, using a microstrip transmission line on a Rogers RT/duroid 5880 substrate with  $\epsilon_r$  of 2.2 and thickness of 0.787 mm. The dimensions of  $W_0$  and  $W_1$  are 2.204 mm and 1.254 mm, which correspond to a microstrip width that yield the impedance of 50 and 70.71  $\Omega$ , respectively. The dimensions are optimized for operation at 8.45 GHz, so that  $L_0$  is 7.00 mm,  $L_1$  is 6.65,  $L_2$  is 7.64 mm and  $R_1$  is a 100  $\Omega$  resistor.

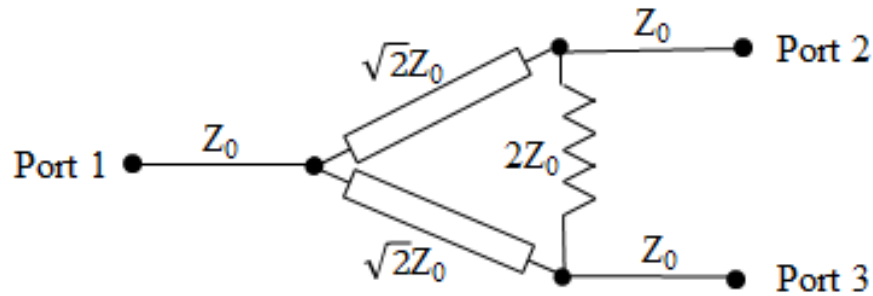


Figure 49. Circuit implementation of the Wilkinson power splitter

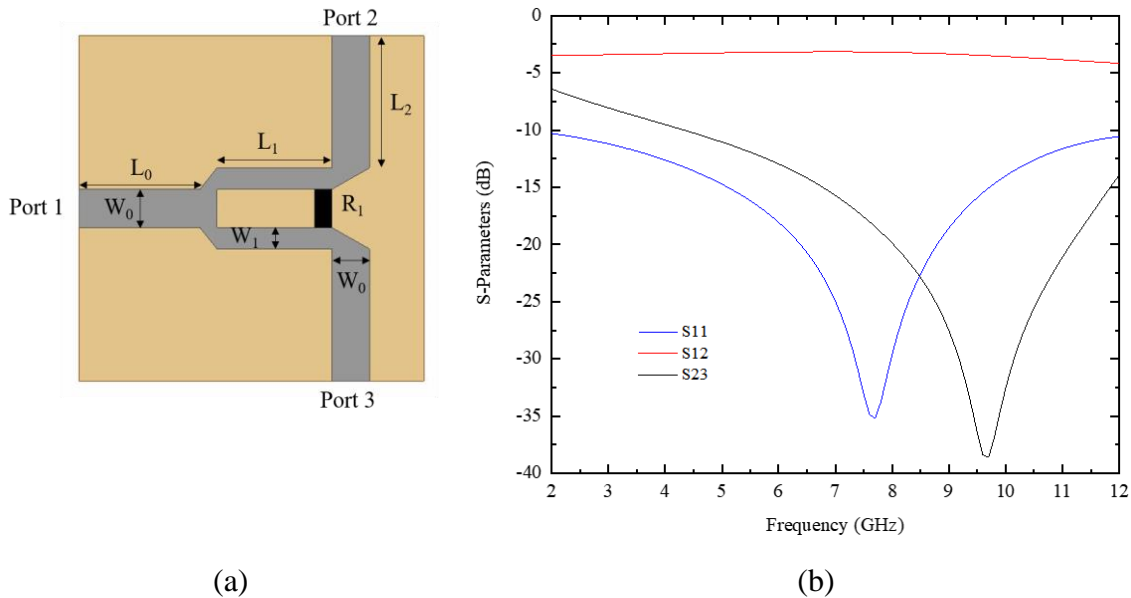


Figure 51. Binomial power splitter on Rogers RT/duroid 5880: (a) diagram and (b) simulated S-parameters

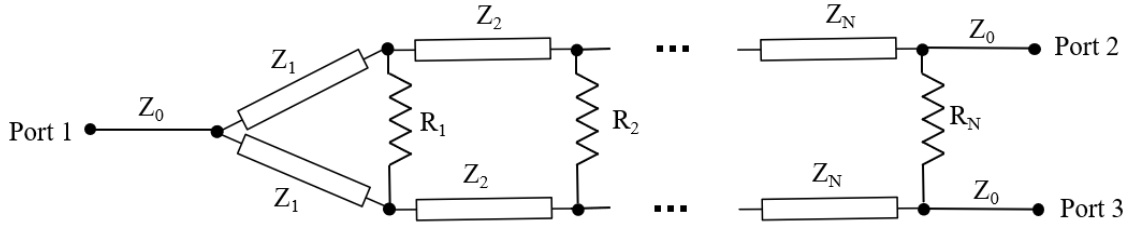


Figure 53. Multi-section Wilkinson power splitter

Table 6. Impedances for multi-section binomial Wilkinson power dividers

Number of Sections	$Z_0$	$Z_1$	$Z_2$	$Z_3$	$Z_4$
1	50 $\Omega$	70.71 $\Omega$			
2	50 $\Omega$	59.46 $\Omega$	84.09 $\Omega$		
3	50 $\Omega$	54.53 $\Omega$	64.84 $\Omega$	84.09 $\Omega$	
4	50 $\Omega$	52.21 $\Omega$	59.46 $\Omega$	64.84 $\Omega$	77.11 $\Omega$
4	50 $\Omega$	52.21 $\Omega$	59.46 $\Omega$	64.84 $\Omega$	77.11 $\Omega$

The divider is matched for operation at 8.45 GHz. The performance of the divider is narrowband, as shown in Figure 34. This occurs due to frequency constraints of the quarter-wave microstrip impedance transformation. As demonstrated in the balun design, modifications can be made to microstrip impedance transformers to improve the bandwidth. One solution, in the case of power splitters, is to utilize an impedance taper to implement a multi-section Wilkinson power splitter [39]. As shown in Figure 54, multiple transmission line impedance transformers and port-matching resistors can be used to modify the power splitter.

One method of creating the multiple sections is to utilize the binomial impedance transformer [34]. As the number of sections in the binomial impedance taper increases, the bandwidth of the transformer increases. Using the following equations, the impedances for the sections can be determined:

$$\ln \frac{Z_{n+1}}{Z_n} \cong 2^{-N} C_n^N \ln \frac{Z_L}{Z_0} \quad (4.31)$$

where  $N$  is the number of sections,  $Z_0$  is the initial impedance,  $Z_N$  is the final impedance, and  $n$  is the integers from 0 to  $N$ , and  $C_n^N$  is the binomial coefficient given as

$$C_n^N = \frac{N!}{(N-n)!n!} \quad (4.32)$$

For an impedance transformation from  $Z_0 = 50 \Omega$  to  $Z_L = 100 \Omega$ , the required impedances are shown in Table 6. Application of the binomial impedance transformer to the Wilkinson power splitter allows for broadband power division. A binomial Wilkinson with divisions of one, two, and three were designed and simulated in HFSS, as shown in Figure 56. Designed for FR4 substrate, the dimensions of the power splitters are given in Table 9 with the same convention as Figure 52(a). The results in Figure 58 show that the addition of each division adds another pole to the S-parameters.

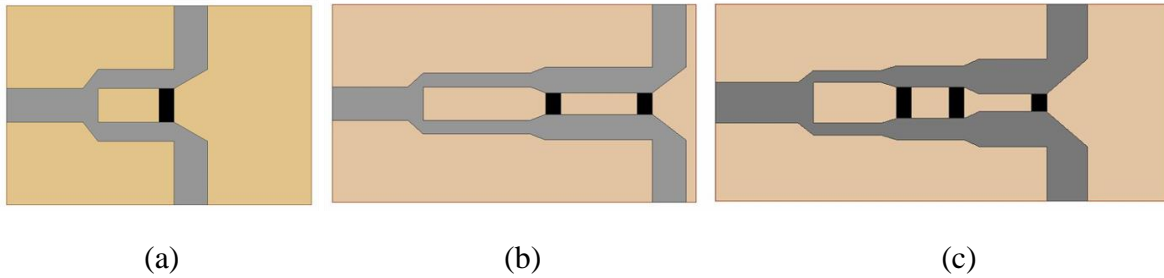


Figure 55. Multi-section binomial Wilkinson power dividers on FR4 substrate with sections of (a) 1, (b) 2 and (c) 3.

Table 9. Dimensions of multi-section binomial Wilkinson power dividers on FR4 substrate

N	$W_0$	$W_1$	$W_2$	$W_3$	$L_0$	$L_1$	$L_2$	$L_3$	$L_4$
1	2.204	1.254	-	-	5	5	4.144	-	-
2	2.204	0.9	1.682	-	5	7.06	7.06	4.1	
3	2.204	0.75	1.245	1.932	5	7.06	7.06	7.06	4.06

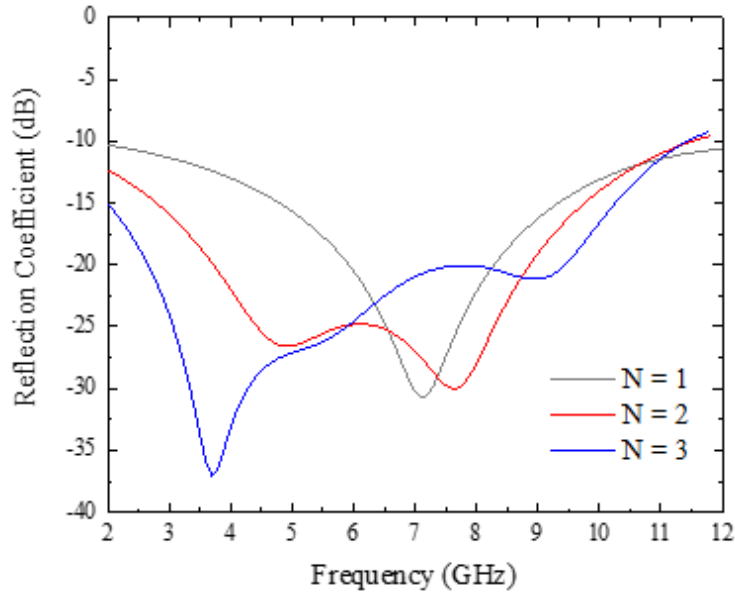


Figure 57. Reflection coefficient of binomial Wilkinson power dividers with number of sections of 1, 2, and 3

To ensure broadband behavior, a binomial Wilkinson with three sections was designed as a microstrip transmission line on Rogers RT/duroid 5880 substrate. The dimensions are optimized for operation at 8.45 GHz, so that  $L_0, L_1, L_2, L_3$  are 5.00mm,  $W_0$  is 2.45 mm,  $W_1$  is 0.96 mm,  $W_2$  is 1.4 mm,  $W_3$  is 2.15 mm,  $R_1$  is 100  $\Omega$ ,  $R_2$  is 180, and  $R_3$  150  $\Omega$ . The values of  $R_1, R_2$ , and  $R_3$  have been rounded to the nearest common resistor value so 0603 surface mount resistors can be used. The results are shown in Figure 60. Due to the binomial Wilkinson approach, wideband behavior has been achieved from 2 to 13 GHz. The insertion loss (S12) at 8.45 GHz is approximately 3.6 dB, where the 3 dB loss is expected due to half of the power from Port 1 being split to Port 2, and the remaining 0.6 dB can be attributed to conductor and dielectric losses.

Because the array has 4 elements, a 1-to-4 divider is required. Therefore, the designed three section Wilkinson power splitters with outputs are concatenated, as shown in Figure 63, to divide power from Port 1 equally to Ports 2, 3, 4, and 5. The insertion loss, at 8.45 GHz is approximately 6.8 dB, where the 6.0 dB loss is expected due to the power split, and the

remaining 0.8 dB can be attributed to conductor and dielectric losses. The isolation between Ports 2 and 3 is less than 10 dB from 2.0 to 13 GHz. Although not pictured, the isolation between all ports shows a similar response.

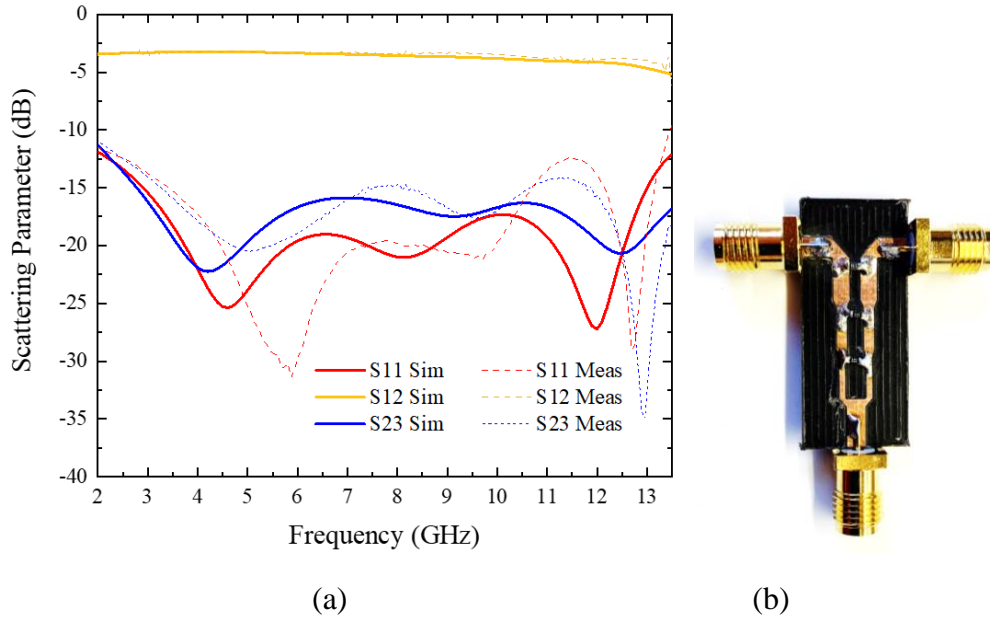


Figure 59. Binomial Wilkinson power divider with three sections: (a) simulated and measured S-parameters and (b) fabricated prototype

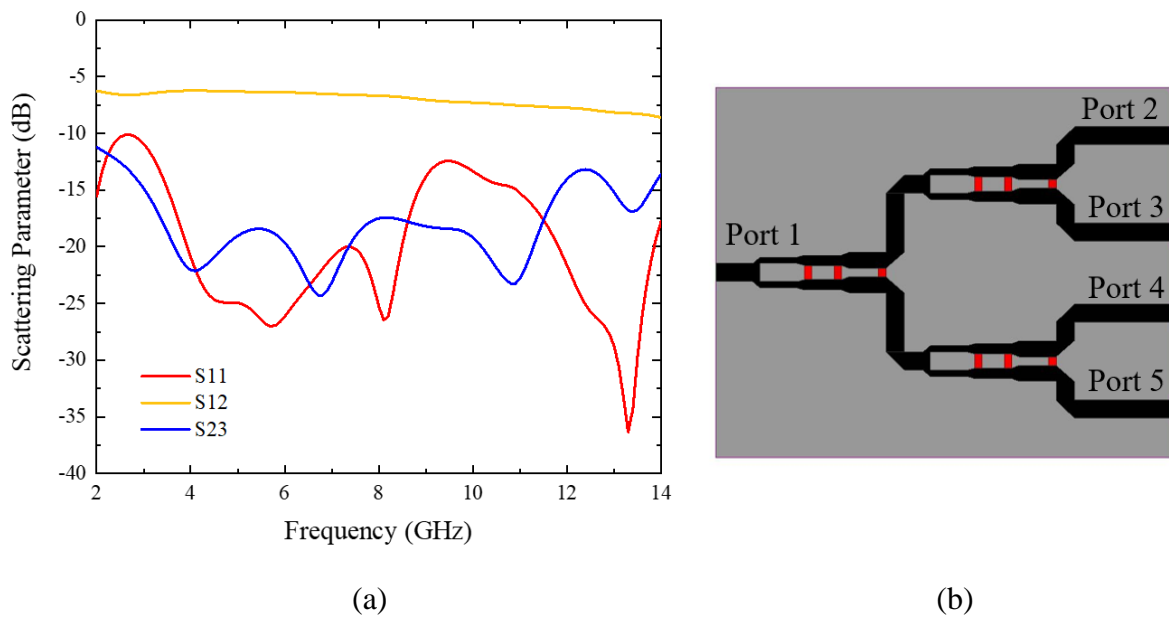


Figure 61. A binomial (3 section) Wilkinson power splitter with four outputs: (a) simulated S-parameters and (b) microstrip implementation



Figure 64. Fabricated copper cavities using (a) electroplating and (b) copper tape

## 4.7 Antenna Characterization

### 4.7.1 Fabrication Process

The designed antennas were fabricated using in-house techniques. The ASA, microstrip balun, and power splitter were milled on Rogers RT/duroid 5880 using the S62 LPKF Milling Machine. For fast prototyping, the backing cavity structure and holding units were fabricated with a common 3D-printing plastic, ABS, using a HICTOP Desktop 3D Printer. The backing cavities were covered in copper tape. Other variations of the backing cavities were fabricated using a standard milling machine out of copper stock. For the final deployable system, electroplating a 3D printed cavity is recommended. This method will reduce weight in comparison to copper stock and increase conductivity in comparison to copper tape. The electroplated cavities can be purchased from a 3D printing company or created in-house. Using a standard electroplating kit, the SWBC was created, as shown in Figure 65. Copper tape was used during antenna characterization due to patina formation on the in-house electroplated cavity.

### 4.7.2 Measurement Process

The following antennas were measured for comparison: ASA, SWBC-ASA, ASA Array, and SWBC-ASA Array. The  $\Gamma$  of the antennas is measured using the Agilent VNA N5230A with a frequency sweep from 1.0 GHz to 10 GHz. The radiation characteristics of the antennas are

measured using a Quietbox AVS 700 Anechoic chamber. The setup is shown in Figure 67. To characterize the RG as a function of frequency, a sweep is performed from 1.0 GHz to 10 GHz. A dual-polarized horn antenna is used to measure the horizontal  $RG_{00}$  magnitude,  $M_H$ , and phase,  $\Phi_H$ , and the vertical  $RG_{00}$  magnitude,  $M_V$ , and phase,  $\Phi_V$ , which can be represented in the complex form as [40]

$$E_H = 10^{M_H/20} e^{j(\Phi_H\pi/180)} \text{ and} \quad (4.33)$$

$$E_V = 10^{M_V/20} e^{j(\Phi_V\pi/180)}. \quad (4.34)$$

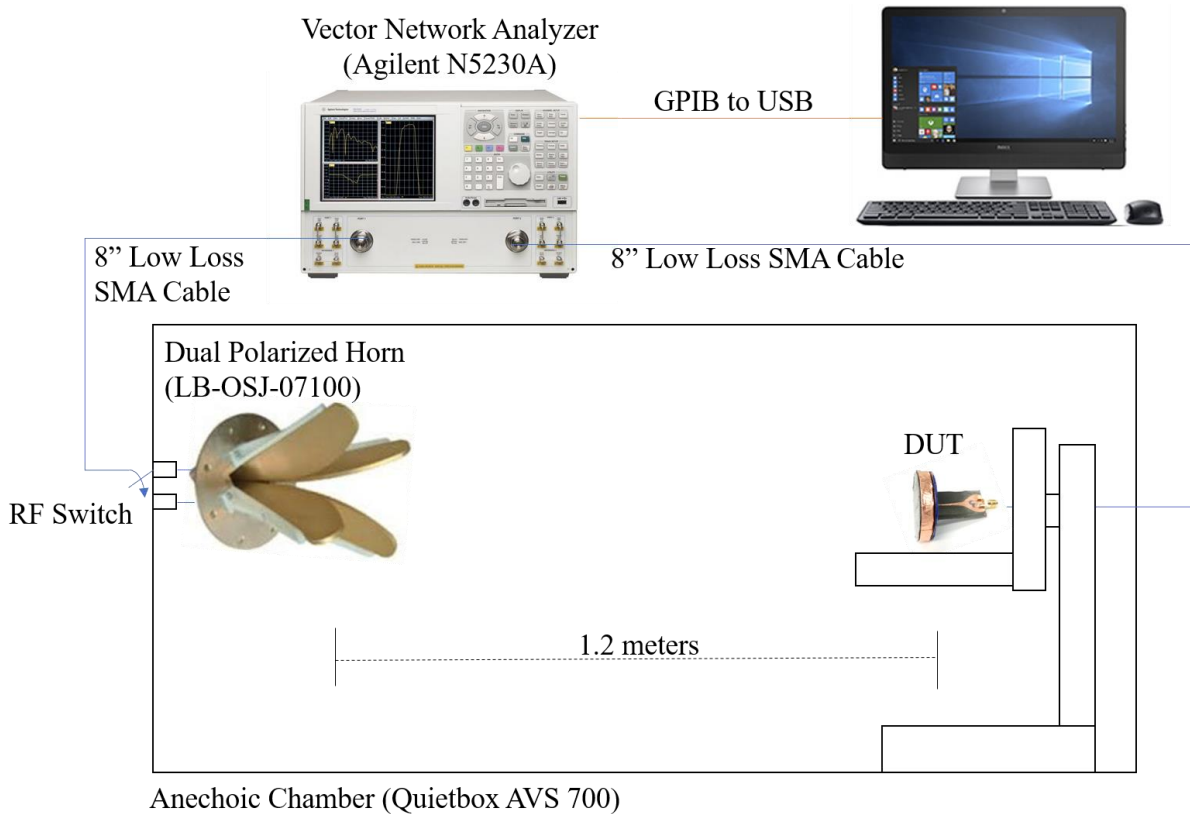


Figure 66. Set-up of Anechoic Chamber (Quietbox AVS 700) for radiation characterization

The total  $RG_{00}$  is then calculated from

$$E_{\text{Total}} = E_R + E_L, \quad (4.35)$$

where  $E_R$  and  $E_L$  are the complex values of the right hand and left hand circularly polarized complex  $RG_{00}$ , calculated according to

$$E_R = \frac{1}{\sqrt{2}}(E_H + jE_V) \text{ and} \quad (4.36)$$

$$E_L = \frac{1}{\sqrt{2}}(E_H - jE_V). \quad (4.37)$$

The axial ratio can be determined by the following ratio of the circularly polarized  $RG_{00}$  as follows,

$$AR \text{ [dB]} = 20 \log_{10} \left( \frac{|E_R| + |E_L|}{|E_R| - |E_L|} \right). \quad (4.38)$$

The data is collected from the Anechoic Chamber software and the conversions are completed using a MATLAB script.

### 4.7.3 Spiral Antennas

Using the described measurement process, the fabricated antenna was characterized for  $|\Gamma|$ ,  $RG_{00}$ , and  $AR_{00}$  from 1.0 to 10 GHz. For a more accurate comparison between measured and simulated results, the antennas are simulated with the 40 mm Klopfenstein balun. The fabricated ASA, as shown in Figure 69, has a measured impedance bandwidth ( $|\Gamma| < -10$  dB) from 2.5 GHz to 10 GHz, which matches simulated results. The measured  $|\Gamma|$  shows degraded performance in terms of magnitude, which is due to discrepancies caused by the solder connections. For additional comparison, the ASA simulation is modified to include the lower conductivity of the solder connections. Solder typically has a conductivity of  $7.0 \times 10^6$  S/m, while copper has a

conductivity of  $5.8 \times 10^7$  S/m. The  $|\Gamma|$  of the modified simulation results match the measured results from 4.5 GHz to 10 GHz.

The  $RG_{00}$  and  $AR_{00}$  of the ASA are shown in Figure 71. The measured  $RG_{00}$  shows a gain of 3.7 to 3.9 dBi from 8.4 to 8.5 GHz, the frequency band of interest. Drops in the measured  $RG_{00}$  at 4.5 GHz and 9.2 GHz are also found in the results of the simulation modified to include the solder connections. The measured  $RG_{00}$  at 8.45 GHz is 3.7 dBi, which is approximately 2.0 dB less than the originally simulated  $RG_{00}$ . The measured  $AR_{00}$  from 7.5 to 10 GHz is above 3.0 dB, which is likely caused by fabrication errors, as the radiation characteristics at higher frequencies depend on accurate spiral dimensions near the feed point.

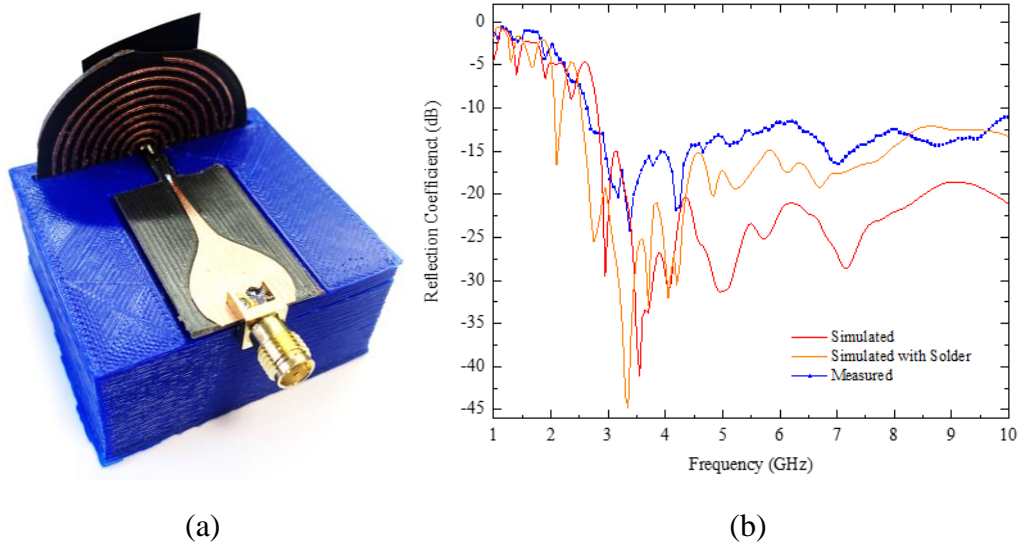


Figure 68. Archimedean spiral antenna: (a) fabricated prototype and (b) measured and simulated reflection coefficient

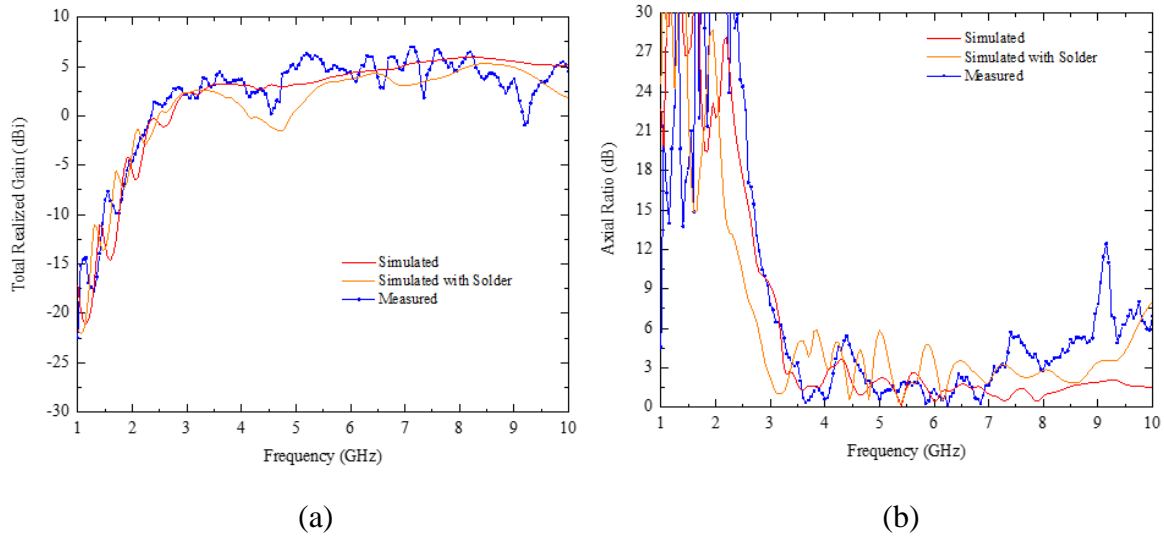


Figure 70. Measured and simulated (a) realized gain and (b) axial ratio at boresight of the Archimedean spiral antenna

The SWBC-ASA is fabricated using the original characterized ASA and balun. The SWCB-ASA, as shown in Figure 73, shows impedance matching from 4.0 to 10 GHz. Comparison to a modified simulation with solder-connections shows that the degraded  $|\Gamma|$  from 8.0 to 10 GHz is caused by the low conductivity of the solder connection.

The radiation characteristics of the SWCB-ASA are shown in Figure 75. The measured  $RG_{00}$  of the SWCB-ASA is well matched to the simulated but shows discrepancies at 4.5 and 9.2 GHz. These discrepancies, as seen previously in the characterized ASA, are attributed to the solder connections. The measured  $RG_{00}$  is 8.6 to 9.3 dBi from 8.4 to 8.5 GHz, which is approximately only 0.8 dB less than the originally simulated  $RG_{00}$ . The measured  $AR_{00}$  is above 3 dB in the measured frequency range. The SWBC-ASA simulation predicts lower AR bandwidth compared to the ASA due to the influence of the cavity. Simulating the SWBC-ASA with solder shows the AR degradation is partially attributed to the solder connection. Additional discrepancies can be attributed to the fabrication variations of the copper-tape and ABS cavity.

The measured and simulated radiation patterns shown in Figure 77 indicate the backing cavity successful reduces the back-lobe radiation. The measured radiation pattern has a HPBW of  $60^\circ$ .

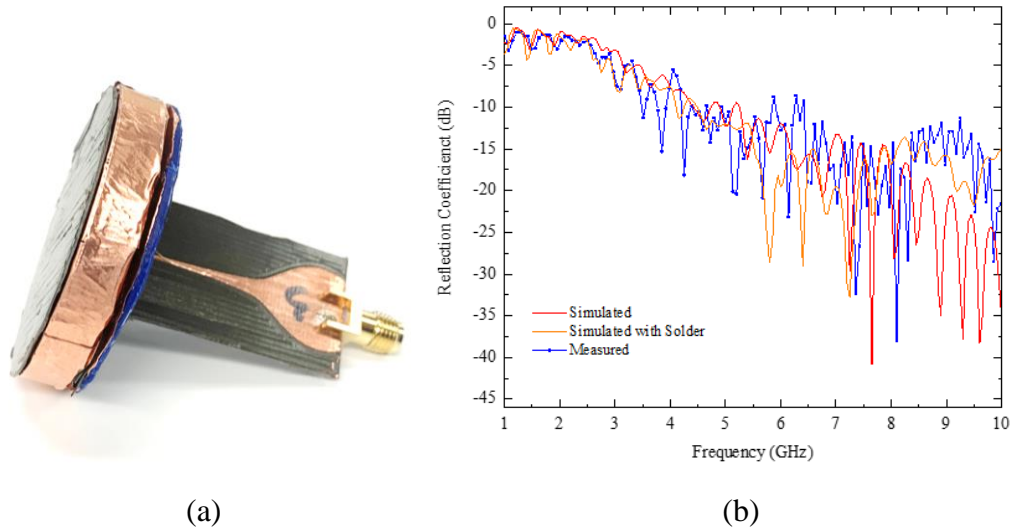


Figure 72. Archimedean spiral antenna with sloped wall backing cavity: (a) fabricated prototype and (b) measured and simulated reflection coefficient

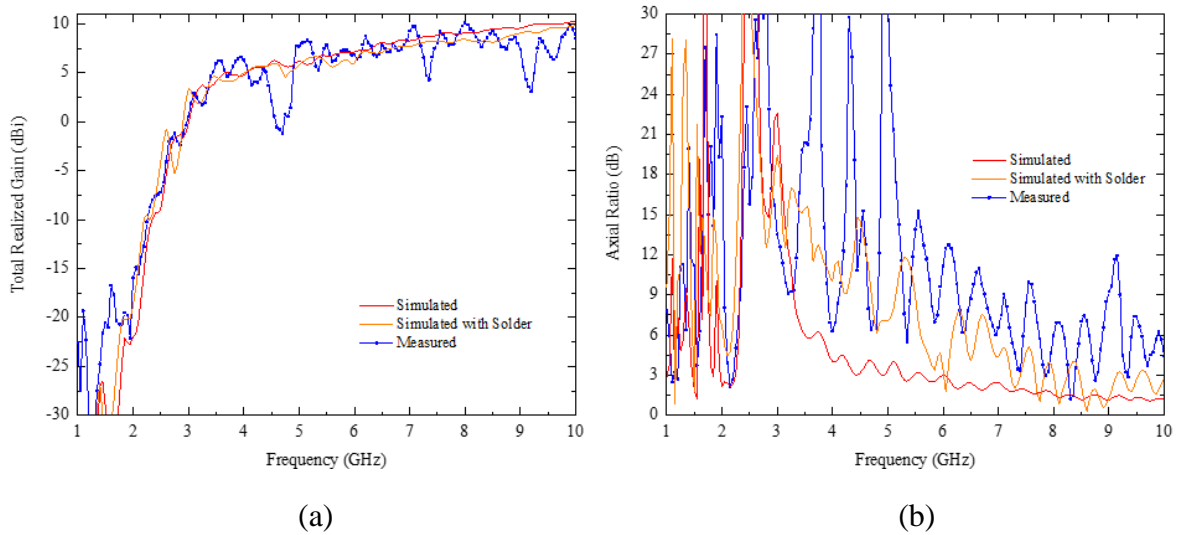


Figure 74. Measured and simulated (a) realized gain and (b) axial ratio at boresight of the Archimedean spiral antenna with sloped wall backing cavity

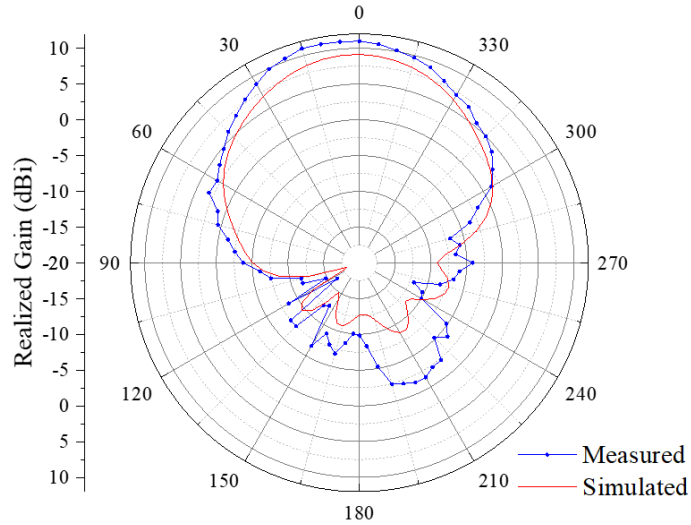


Figure 76. Measured and simulated realized gain radiation pattern as a function of  $\theta$  at  $\phi = 0^\circ$  of the Archimedean spiral antenna with sloped wall backing cavity

#### 4.7.4 Arrays

The fabricated antenna arrays were characterized for  $|\Gamma|$ ,  $RG_{00}$ , and  $AR_{00}$  from 1.0 to 10 GHz. The corresponding antenna array simulations include the Klopfenstein baluns. The S-parameters of the Wilkinson binomial power splitter are extracted and combined with the S-parameters of the antenna array in Keysight ADS. The ASA array, as shown in Figure 79, has a measured  $|\Gamma|$  below -10 dB from 4.5 to 9 GHz. The  $RG_{00}$  and  $AR_{00}$  of the ASA array are shown in Figure 81. The measured  $RG_{00}$  shows a gain of 9.8 to 10.4 dBi from 8.4 to 8.5 GHz, which is approximately 2.0 dB less than the simulated  $RG_{00}$ . The measured  $AR_{00}$  from 7.5 to 10 GHz is above 3.0 dB, which is likely caused by fabrication errors.

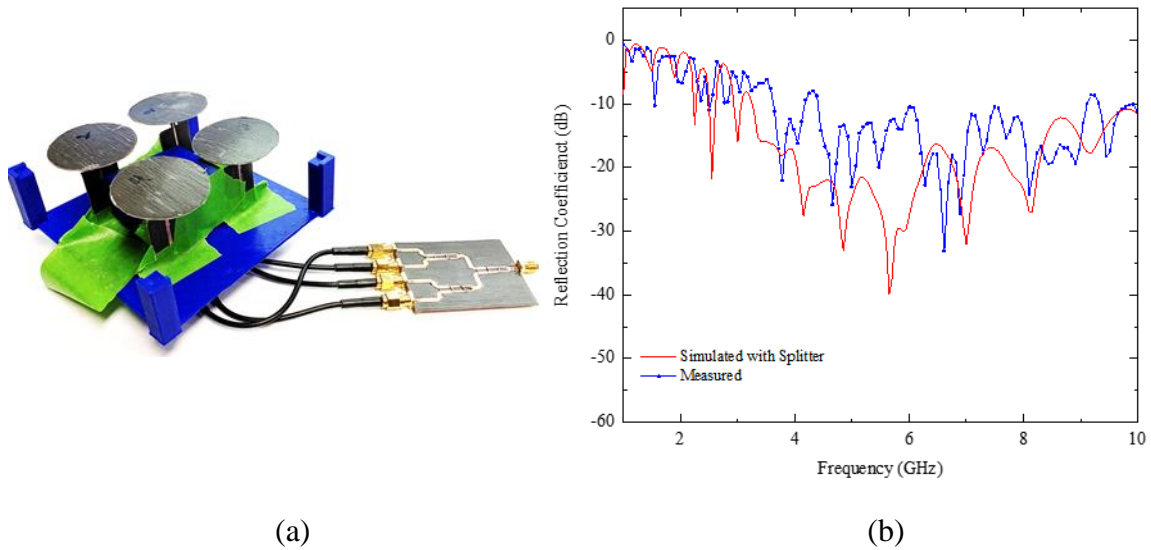


Figure 78. Archimedean spiral antenna array (a) prototype and (b) measured and simulated reflection coefficient

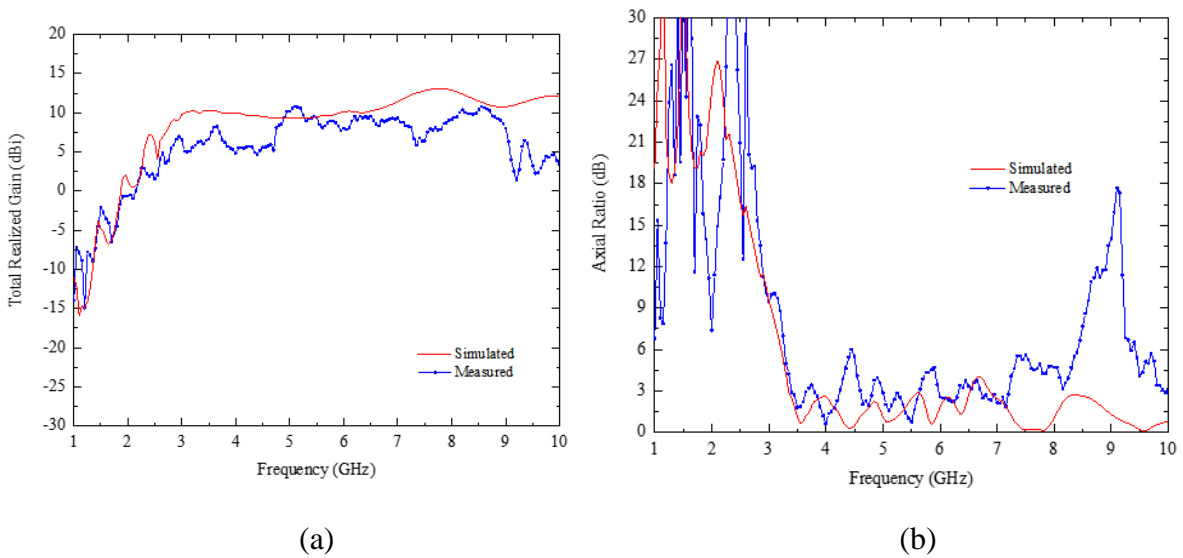


Figure 80. Measured and simulated (a) realized gain and (b) axial ratio at boresight of the Archimedean spiral antenna array

The baluns and power splitter for SWCB-ASA array, shown in

Figure 16, require a volume of 0.5U. The measured S-parameters of the fabricated array show impedance matching from 4.0 to 10 GHz, as shown in Figure 83. In Figure 85, the measured  $RG_{00}$  shows a gain of 13.5 to 14.26 dBi from 8.4 to 8.5 GHz, which is approximately

2.3 dB less than the simulated  $RG_{00}$ . The balun effect degrades the  $AR_{00}$ . The measured and simulated radiation patterns shown in Figure 87 indicate the backing cavity successfully reduces the back-lobe radiation. The measured and simulated radiation patterns have a HPBW of  $20^\circ$ . In the measured radiation pattern, the back-lobe radiation is attributed to leakage from the power splitter and balun, rather than back-lobe radiation of the spiral antennas. The measured characteristics of the SWBC-ASA array indicate the impedance BW was maintained even with the effect of the power splitters, balun, and solder connections. However, the fabrication errors caused significant degradation in the  $RG_{00}$  and  $AR_{00}$ .

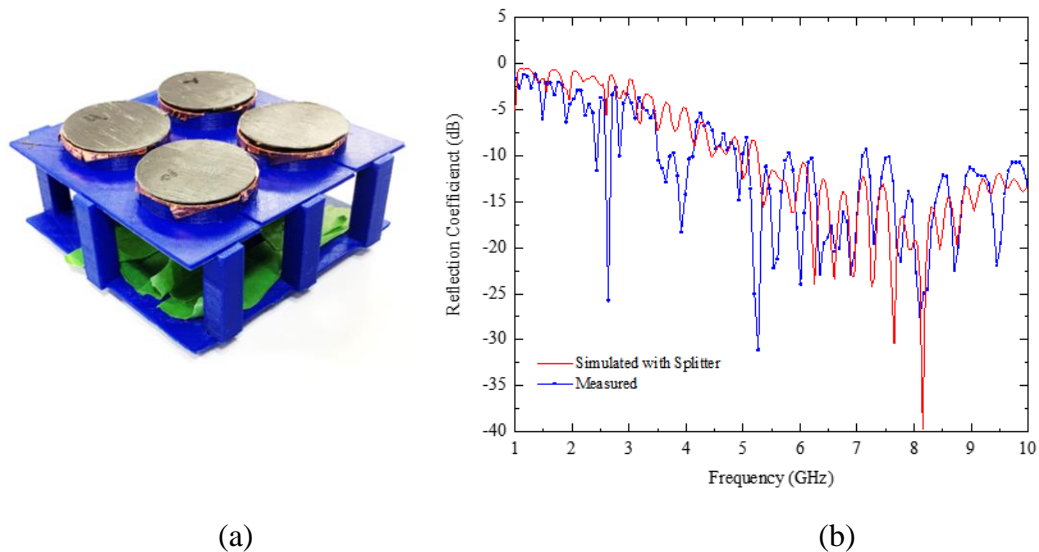


Figure 82. Archimedean spiral antenna array with sloped wall backing cavity: (a) prototype and (b) measured and simulated reflection coefficient

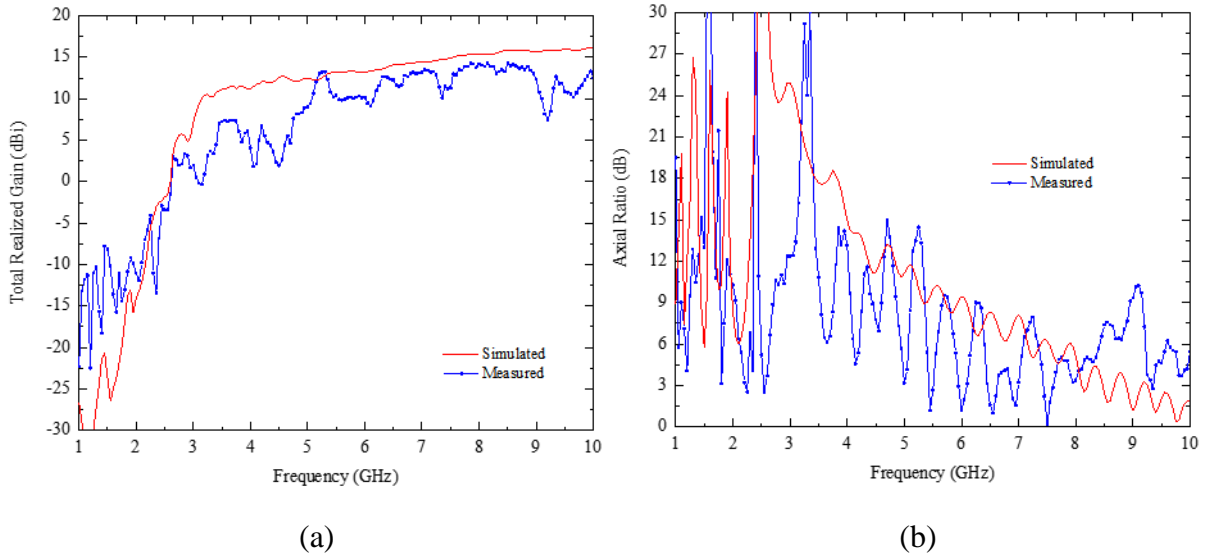


Figure 84. Measured and simulated (a) realized gain and (b) axial ratio at boresight of the Archimedean spiral antenna array with sloped wall backing cavity

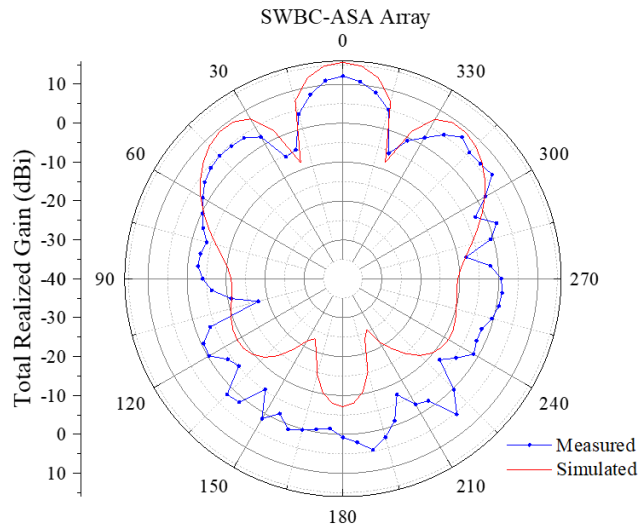


Figure 86. Measured and simulated realized gain radiation pattern of the Archimedean spiral antenna array with sloped wall backing cavity

## CHAPTER 5: TRANSMITTER DESIGN

To fulfill the link budget, it is required that the communication system be capable of transmitting at a power of 37 dBm with a bandwidth of 1.0 GHz. In this section, a design is proposed for X-band communication system based on COTS. The selection of components and frequency conversions will be explained.

Recommendations are made on the design of an X-Band transmitter. Similar attempts at custom design and fabrication of high data rate transmitters have been undertaken by universities for CubeSat projects. For example, at the University of Colorado, Boulder, a CubeSat communications system was designed to be compatible with the NASA Near Earth Network and provide a 12.5 Mbps X-band downlink [41]. In this thesis, using Keysight's Advanced Design System (ADS), a basic transmitter has been implemented to fit the link budget requirements. The design utilizes COTS components, allowing for faster development of the system. The modulator of the system is software-defined and implemented by a Field-Programmable Gate Array (FPGA) and Digital to Analog Convertor (DAC). The X-band direct-conversion transmitter is shown in Figure 89.

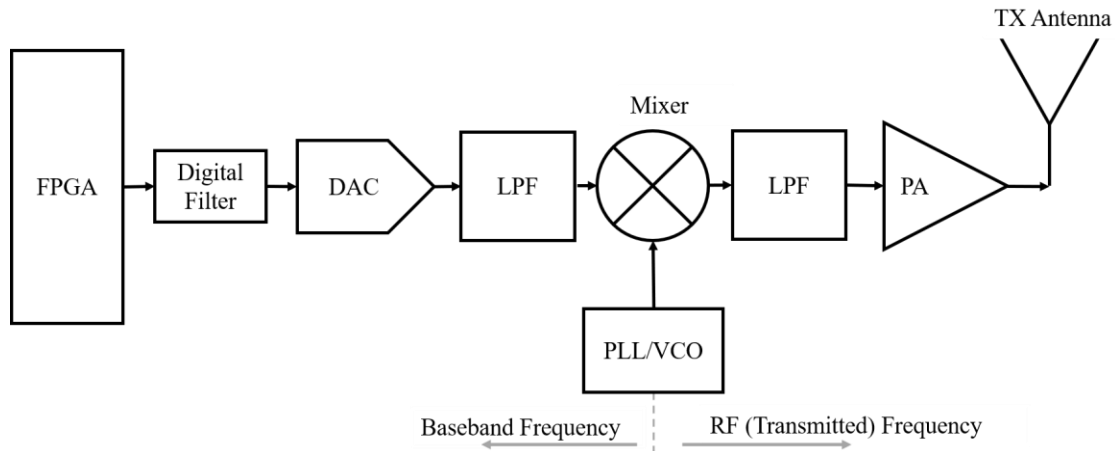


Figure 88. X-band transmitter schematic employing direct frequency conversion

### 5.1 Modulation

Using Keysight Advanced Design System (ADS), an OQPSK modulator was simulated. The schematic is shown in Figure 91, which implements the hardware discussed in Chapter 3 Modulation Selection. An envelope simulation is used to analyze the effects of phase modulation in the time and frequency domain. Using ADS, the real part of the modulated radio frequency (RF) carrier in the time domain, the spectrum of the generated signal, and the constellation diagram were found, as shown in Figure 93. This modulation scheme can be implemented using an FPGA.

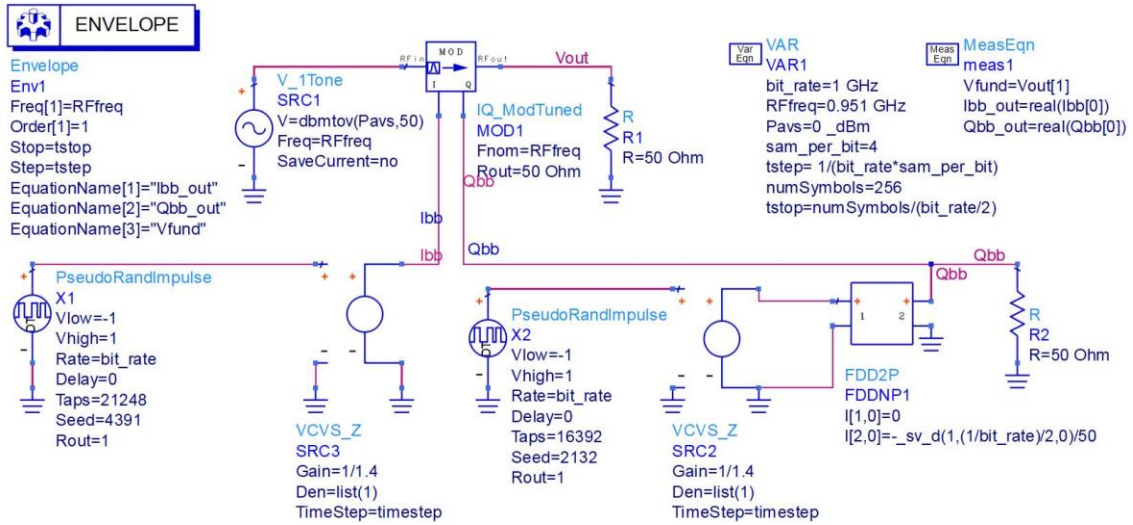


Figure 90. ADS implementation of OQPSK modulation

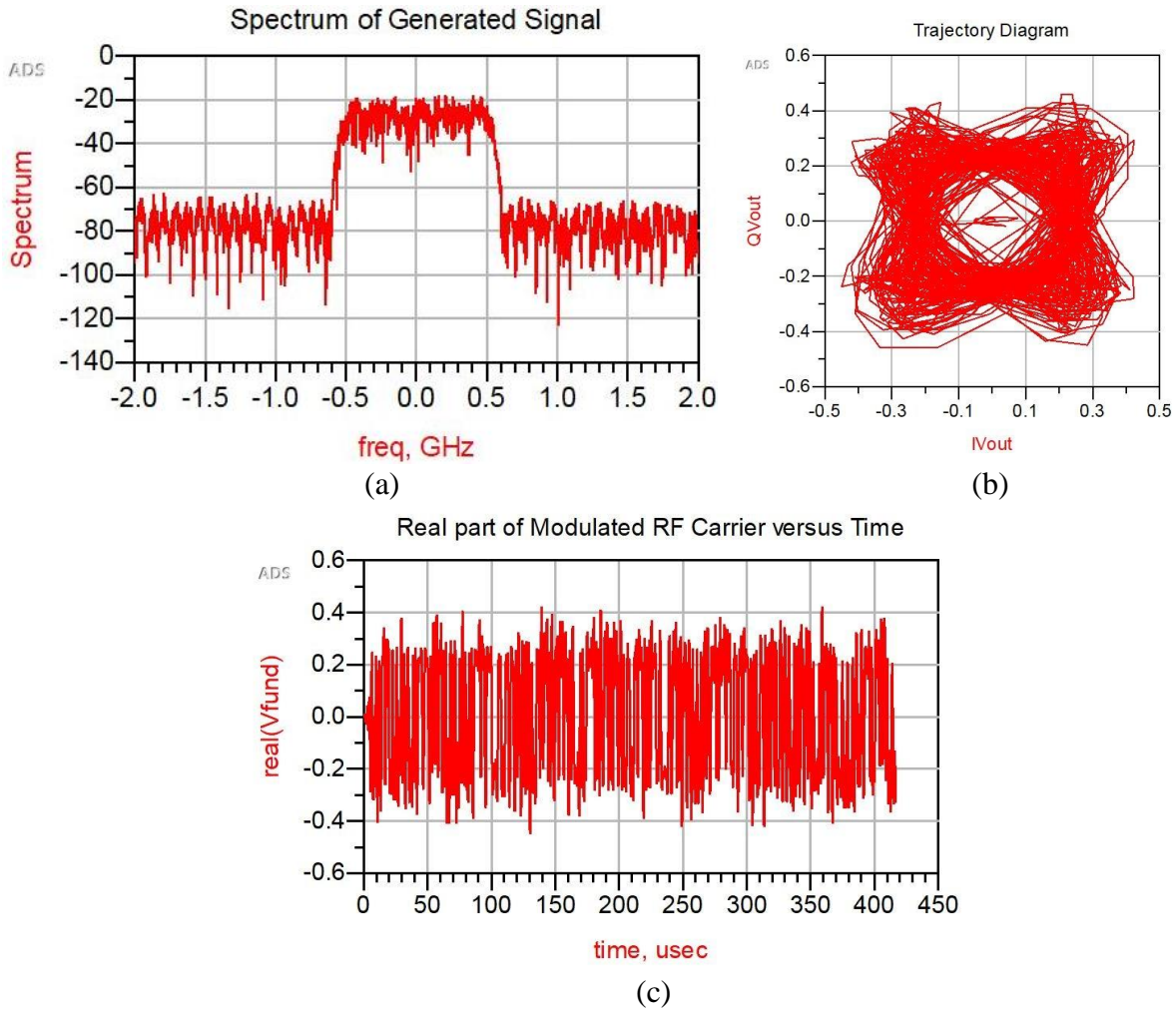


Figure 92. OQPSK simulation results for (a) spectrum of generated signal, (b) trajectory diagram, and (c) real part of modulated RF carrier versus time.

## 5.2 Digital to Analog Converter

The digital OQPSK signal generated by the FPGA is converted to analog via a Digital to Analog Converter (DAC). Conventionally, the DAC can bottleneck the data rate in a software-based radio. Therefore, a high data rate DAC must be selected for this application. For example, the Texas Instruments DAC38RF89 can operate as an 8-bit DAC with 9.0 Gbps data rate capabilities [42]. It can synthesize signals from 0 to 4.5 GHz. The design of the system must also consider the frequency spurs that occur in the signals generated by DACs. The ratio of the fundamental frequency content to the unwanted spurs is termed the Spurious-free dynamic range (SFDR). The selected DAC operates with a 93 dBc SFDR at 951 MHz RF output within 500 MHz of the RF output. A filter can be used to remove the noise introduced by the DAC.

## 5.3 Upconversion

Due to the low frequency output from the DAC, a mixer is required to upconvert the frequency from 951 MHz. In this case, the mixer utilizes a local oscillator with frequency of 7499 MHz. The mixer outputs two fundamental frequencies, 8450 MHz and 6548 MHz. A filter will be used to select the desired frequency of 2400 MHz. A simplified implementation of this upconversion is implemented in ADS and solved using the harmonic balance simulation. The results of the frequency content are shown in Figure 94.

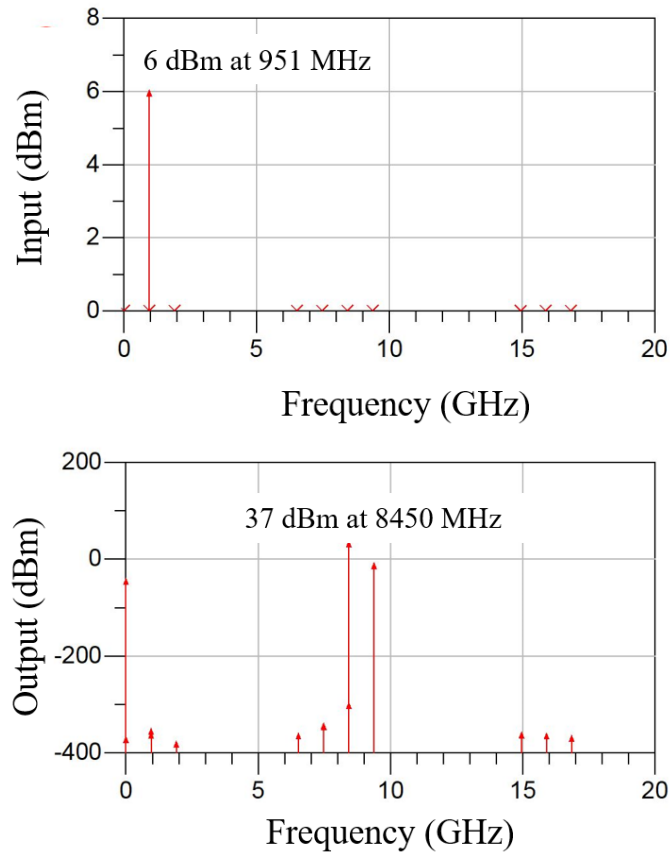


Figure 94. Simulated spectrum of (a) input and (b) output voltages of the ideal direct frequency conversion X-Band transmitter in ADS

#### 5.4 Amplification

Finally, a power amplifier is implemented to increase the gain of the signal. A Gallium nitride (GaN) X-band power amplifier (Plextek RFI) is chosen to allow for a transmitting power of 5W at a drain efficiency of 55% [43]. Due to the nonlinearity of the amplifier, unwanted spectral content may be introduced, so a filter is added.

## CHAPTER 6: CONCLUSION

In this thesis, a wideband X-band communications system was developed for CubeSat lunar orbit applications. A survey of the current state of deep space CubeSats and their communications systems revealed a demand for innovation, especially by student-led CubeSat groups. To fulfill the requirements of a lunar tube exploration mission, the modulation, frequency, and bandwidth were selected for the system to be OQPSK, X-band, and a wide bandwidth of  $> 1.0$  GHz, respectively. Using these parameters and the known performance of the receiving ground stations of the DSN, a link budget was calculated. A gain of 15 dBi is required to achieve a BER of  $10^{-4}$  at 400,000 km. To achieve this, a two-arm ASA array was designed. Several techniques were used in the design of the array, including a Klopfenstein impedance taper for the balun and binomial matching sections for the Wilkinson power splitter. Notably, a novel backing cavity was designed with sloped walls to mitigate the effect of the destructive interference caused by the height of the cavity. The SWBC-ASA array was fabricated and characterized using in-house equipment. The measured results were found to match the simulation, with differences in  $RG_{00}$  and  $AR_{00}$  being due to fabrication errors. Lastly, a transmitter was designed and simulated to achieve a transmitting power of 37 dBm and bandwidth of 1.0 GHz. Overall, this thesis provided the basis for the development of a high-data rate communication system for the University of Alabama's potential deep space CubeSat.

Recommendations for future work include increasing the size and gain of the ASA array. A deployable antenna array may provide significant gain if the CubeSat can afford the added complexity and volume. Additionally, optimization can be performed to miniaturize the size of

the individual baluns, antenna elements, and power splitter to make better use of the space available. In terms of the transmitter, future research must include analysis of the linearity and stability of the transmitter. The electromagnetic compatibility of the communication system with the other CubeSat subsystems should be investigated, especially the power subsystem, during integration. Additionally, the CubeSat subsystem requires radiation hardening, random vibration, thermal vacuum bakeout, and shock testing.

## REFERENCES

- [1] G. Brown and W. Harris, "How Satellites Work," HowStuffWorks.com, 19 May 2000. [Online]. [Accessed 1 February 2020].
- [2] Jet Propulsion Laboratory, "Mars Cube One (MarCO)," September 2018. [Online]. Available: [https://mars.nasa.gov/internal\\_resources/344/](https://mars.nasa.gov/internal_resources/344/). [Accessed January 1 2020].
- [3] "About: The Cubesat Program," California Polytechnic State University, [Online]. Available: <https://www.cubesat.org/about>. [Accessed 1 February 2020].
- [4] S. Antunes, "Your Own Satellite: 7 Things to Know Before You Go," 11 April 2014. [Online]. Available: <https://makezine.com/2014/04/11/your-own-satellite-7-things-to-know-before-you-go/>. [Accessed 1 January 2020].
- [5] "CubeSat Design Specification Rev. 13," 2014. [Online]. Available: <https://www.cubesat.org/resources>. [Accessed 1 January 2020].
- [6] B. Klofas, A. Jason and L. Kyle, "A Survey of CubeSat Communication Systems," in *CubeSat Developers' Workshop*, Utah, 2008.
- [7] M. Swartwout, "The First One Hundred CubeSats: A Statistical Look," *Journal of Open Source Software*, vol. 2, no. 2, pp. 213-233, 2013.
- [8] T. Villela, C. A. Costa and A. M. Brandao, "Towards the THousandth CubeSat: A Statistical Overview," *International Journal of Aerospace Engineering*, pp. 1-13, January 2019.
- [9] E. Kulu, "Nanosats Database," [Online]. Available: <https://www.nanosats.eu/>. [Accessed 26 January 2020].
- [10] NASA CubeSat Launch Initiative, "CubeSat 101: Basic Concepts and Processes for First-Time CubeSat Developers," NASA, 2017.
- [11] "Hera," ESA.int, [Online]. Available: [https://www.esa.int/Safety\\_Security/Hera/Hera](https://www.esa.int/Safety_Security/Hera/Hera). [Accessed 1 February 2020].
- [12] N. Chahat, "Advanced CubeSat Antennas for Deep Space and Earth Science Missions: A review," *IEEE Antennas and Propagation Magazine*, vol. 61, no. 5, pp. 37-46, Oct 2019.

- [13] "Voyager: High-Gain Antenna," JPL, [Online]. Available: <https://voyager.jpl.nasa.gov/mission/spacecraft/instruments/hga/>. [Accessed 1 January 2020].
- [14] "Top Five Technologies Needed for a Spacecraft to Survive Deep Space," NASA, 17 Sept 2019. [Online]. Available: <https://www.nasa.gov/feature/top-five-technologies-needed-for-a-spacecraft-to-survive-deep-space>. [Accessed 1 January 2020].
- [15] Jet Propulsion Laboratory, "Iris V2.1 CubeSat Deep Space Transponder," California Institute of Technology, 2016. [Online]. Available: [https://www.jpl.nasa.gov/cubesat/pdf/Brochure\\_IrisV2.1\\_201611-URS\\_Approved\\_CL16-5469.pdf](https://www.jpl.nasa.gov/cubesat/pdf/Brochure_IrisV2.1_201611-URS_Approved_CL16-5469.pdf). [Accessed November 1 2019].
- [16] Soderman/NLSI Staff, "Marius Hills pit offers potential location for lunar base," NASA, [Online]. Available: <https://sservi.nasa.gov/articles/lava-tube-lunar-base/>. [Accessed 1 March 2020].
- [17] R. Walker, "Deep-space CubeSats: Thinking inside the box," *Astronomy & Geophysics*, vol. 59, pp. 5.24-5.30, 2018.
- [18] CCSDS Secretariat, "Proceedings of the CCSDS RF And Modulation Subpanel 1E Meeting of May 2001 Concerning Bandwidth-Efficient Modulation," Consultative Committee for Space Data Systems, Oxfordshire, U. K., 2001.
- [19] R. E. Ziemer and W. H. Tranter, "Advanced Data Communications Topics," in *Principles of Communications: Systems, Modulation, and Noise*, Wiley, 2014, pp. 477-563.
- [20] A. Kwok, "DSN Telecommunications Link Design Handbook: 206, Rev. B Telemetry General Information," California Institute of Technology, 2009.
- [21] M. S. Reid, "Low-Noise Systems in the Deep Space Network," Jet Propulsion Laboratory, 2008.
- [22] Berner, J. Berner, T. Pham, A. M. Bhanji and C. Scott, "Deep Space Network Services Catalog," Jet Propulsion Laboratory, 2015.
- [23] D. J. Mulally and D. K. Lefevre, "A Comparison of Digital Modulation Methods for Small Satellite Data Links," Cynetics Corporation, Rapid City, SD, 1991.
- [24] O. Popescu, "Power Budgets for CubeSat Radios to Support," *IEEE Access*, vol. 5, pp. 12618-12625, 2017.
- [25] J. Taylor, "The Deep Space Network: A Functional Description," in *Deep Space Communications*, John Wiley & Sons, Inc., 2016, pp. 15-36.
- [26] C. A. Balanis, *Antenna Theory: Analysis and Design*, 4 ed., Wiley, 2016.
- [27] W. Lee, K. Cho, D. Yoon and K. Hyun, "Design and Performance Analysis of Downlink in Space Communications," *Journal of Astronomy & Space Sciences*, no. 27, pp. 11-20, 2010.

- [28] T. McIntyre, "Space Communication Rates at Multi-Gbps," 28 October 2011. [Online]. Available: [https://pcos.gsfc.nasa.gov/studies/rfi/McIntyre-Todd-RFI\(1\).pdf](https://pcos.gsfc.nasa.gov/studies/rfi/McIntyre-Todd-RFI(1).pdf). [Accessed 1 February 2020].
- [29] J. Dyson, "The equiangular spiral antenna," *IRE Transactions on Antennas and Propagation*, vol. 7, no. 2, pp. 181-187, April 1959.
- [30] R. DuHamel and D. Isbell, "Broadband logarithmically periodic antenna structures," *1958 IRE International Convention Record*, pp. 119-128, 1957.
- [31] J. Kaiser, "The Archimedean two-wire spiral antenna," *IRE Transactions on Antennas and Propagation*, vol. 8, no. 3, pp. 312-323, May 1960.
- [32] M. H. El-Feshawy and H. F. Hammad, "Comparison between broadband equiangular and archimedean spiral rectennas for energy harvesting," in *2016 33rd National Radio Science Conference*, Aswan, 2016.
- [33] R. Bawer and J. Wolfe, "The spiral antenna," *IRE International Convention Record*, pp. 84-95, 1960.
- [34] D. M. Pozar, *Microwave Engineering*, 4 ed., John Wiley & Sons, 2015.
- [35] R. W. Klopfenstein, "A Transmission Line Taper of Improved Design," *Proceedings of the IRE*, vol. 44, no. 1, pp. 31-35, Jan. 1956.
- [36] R. P. Hecken, "A Near-Optimum Matching Section without Discontinuities," *IEEE Trans. Microw. Theory Tech.*, vol. 20, no. 11, pp. 734-739, 1972.
- [37] P. L. Carro and J. de Mingo, "Analysis and Synthesis of Double-Sided Parallel-Strip Transitions," *IEEE Transactions on Microwave Theory and Techniques*, vol. 58, no. 2, pp. 372-380, Feb 2010.
- [38] P. I. Carro, J. de Mingo, P. Garcia-Ducar and C. Sanchez, "Synthesis of Hecken-tapered microstrip to Parallel-Strip baluns for UHF frequency band," in *2011 IEEE MTT-S International Microwave Symposium*, Baltimore, MD, 2011.
- [39] B. Mishra, A. Rahman and S. Shaw, "Design of an ultra-wideband Wilkinson power divider," in *2014 First International Conference on Automation, Control, Energy and Systems*, 2014.
- [40] C. J. Brochu, G. A. Morin and J. W. Moffat, "Gain measurements of a cavity-backed spiral antenna from 4 to 18 GHz using the three-antenna method," Defence Research Establishment Ottawa, Ottawa, 1998.
- [41] S. E. Palo, "High rate communications systems for CubeSats," in *2015 IEEE MTT-S International Microwave Symposium*, Phoenix, AZ, 2015.
- [42] "DAC38RF89," Texas Instruments, [Online]. Available: <http://www.ti.com/product/DAC38RF89>. [Accessed 1 February 2020].

[43] Plextek RFI, "5W X-Band GaN Power Amplifier Using a Commercially Available Discrete Plastic Packaged SMT Transistor," [Online]. Available: <https://www.plextekrfi.com/wp-content/uploads/5W-GaN-PA-using-SMT-discrete.pdf>. [Accessed 1 February 2020].